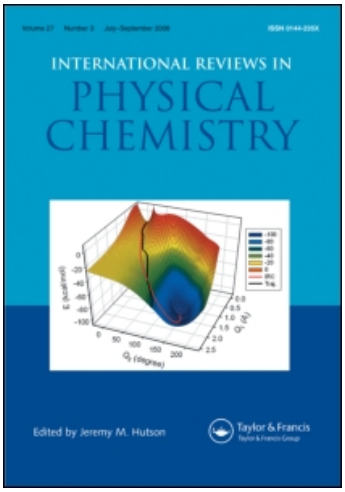

International Reviews in Physical Chemistry
Publication details, including instructions for authors and subscription information:
http://www.informaworld.com/smpp/title~content=t713724383

Fragmentation of rare-gas clusters ionized by electron impact: new theoretical developments and comparison with experiments

David Bonhommeau[a]; Nadine Halberstadt[b]; Udo Buck[c]
[a] Department of Chemistry, University of Minnesota, Minneapolis, MN 55455, USA [b] Laboratoire Collisions, Agrégats, Réactivité, IRSAMC, UMR 5589 CNRS and Université Paul Sabatier, F-31062 Toulouse Cedex 09, France [c] Max-Planck Institut für Dynamik und Selbstorganisation, D-37073 Göttingen, Germany

To cite this Article Bonhommeau, David , Halberstadt, Nadine and Buck, Udo(2007) 'Fragmentation of rare-gas clusters ionized by electron impact: new theoretical developments and comparison with experiments', International Reviews in Physical Chemistry, 26: 2, 353 — 390
To link to this Article: DOI: 10.1080/01442350701223045
URL: http://dx.doi.org/10.1080/01442350701223045

International Reviews in Physical Chemistry,
Vol. 26, No. 2, April–June 2007, 353–390

Taylor & Francis
Taylor & Francis Group

Fragmentation of rare-gas clusters ionized by electron impact: new theoretical developments and comparison with experiments

DAVID BONHOMMEAU†, NADINE HALBERSTADT*‡ and UDO BUCK§

†Department of Chemistry, University of Minnesota, 207 Pleasant Street S.E., 230 Smith Hall, Minneapolis, MN 55455, USA
‡Laboratoire Collisions, Agrégats, Réactivité, IRSAMC, UMR 5589 CNRS and Université Paul Sabatier, 118 route de Narbonne, F-31062 Toulouse Cedex 09, France
§Max-Planck Institut für Dynamik und Selbstorganisation, Bunsenstr. 10, D-37073 Göttingen, Germany

(*Received 16 November 2006; in final form 11 January 2007*)

The fragmentation of rare-gas clusters Rg_n ($2 \leq n \leq 14$ and Rg = Ne, Ar and Kr) following electron-impact ionization is reviewed, with a focus on the comparison of experiment and theory. The most pertinent results are selected in this view, i.e. experiments with size selection of the neutral clusters and simulations taking into account all the relevant electronic states of the ions and their couplings. Simulation results obtained for argon and krypton clusters are compared to abundances determined by experiments. Very good qualitative agreement is found for both types of clusters, concerning the extensive character of the dissociation and the tendency to form larger fragments when the parent ion size increases. For instance, no trimer fragments are found for clusters smaller than the pentamer. In addition, very good quantitative agreement is obtained for argon clusters, especially if the possibility for secondary ionization of the neutral monomer fragments is taken into account. On the other hand, some discrepancies are found between experiment and theory for krypton clusters. Even though the experimental results for the sum of the monomer and dimer ionic fragment proportions are well reproduced in the simulation, there is a disagreement concerning the relative proportion of monomers and dimers. The experiment shows a large predominance of monomers which is not found in the simulation. Several possible reasons for this difference are discussed. The simulation results for neon, argon, and krypton cluster ionization are analysed in detail and provide crucial information on the kinetics of the fragmentation and its mechanism. It is shown that parent ion dissociation occurs within the first picoseconds, and that most of the dynamics is completed within 10 picoseconds. However, the existence of long-lived (more than 100 picoseconds) intermediate species is revealed for clusters larger than hexamers, which are shown to preferentially lead to larger fragments. New results rationalizing the parent ion lifetime dependence with size in terms of the number of coupled electronic states and the symmetry of the neutral precursor are presented. Internal energy distributions and the number of fragmentation events are shown to characterize the fragmentation mechanism as explosive rather than evaporative. The effect of the spin–orbit coupling on the different aspects of the fragmentation process is also examined.

*Corresponding author. Email: Nadine.Halberstadt@irsamc.ups-tlse.fr

International Reviews in Physical Chemistry
ISSN 0144–235X print/ISSN 1366–591X online
http://www.tandf.co.uk/journals
DOI: 10.1080/01442350701223045

Contents PAGE

1. Introduction

Atomic and molecular clusters are a well-established research field with properties between those of single molecules and the condensed phase. What is investigated is the development of characteristic properties as a function of their size. The results are especially well suited for the explanation of macroscopic effects on a molecular level, which are difficult to access in the condensed phase. They also provide new features of both basic behaviour and interesting applications which can be traced back to their finite size [1]. Thus it is not surprising that fragmentation processes which occur during the ionization of neutral clusters played historically a crucial role when they were realized in the 1980s. They destroyed the dream of a straightforward and simple detection of the neutral clusters in a mass spectrometer, which was taken for granted in a series of articles at that time. The origin of the fragmentation is a typical concept of molecular physics. Upon ionization the cluster undergoes an

important structural relaxation which is usually combined with a substantial energy release which, in turn, leads to the evaporation of atoms or molecules [2]. A characteristic example of structural relaxation is the ionization of the weakly bound van der Waals molecule Ar_2 which leads to the strongly bound Ar_2^+ ion with a considerably smaller equilibrium distance and a much deeper well depth. This process is independent of the type of ionization and does not require any excess energy. Since ionization is very fast compared to nuclear motions, Ar_2^+ is created near the equilibrium geometry of the neutral dimer, and therefore with a considerable amount of internal energy. Similar processes occur also for larger clusters and the relaxation of internal energy leads to fragmentation.

Although these considerations were known for some time [3–6], a convincing experimental proof was missing. For such a demonstration the neutral clusters have to be labelled independently of the detection process. One possibility is to use vibrational or rotational spectroscopic fingerprints [7–9]. Another method is based on resonant two-photon ionization [10–12] in which the excited electronic state is chosen to be cluster specific. Usually these methods are restricted to special transitions in dimers or very small clusters. A more general method is to scatter the cluster beam from a light atomic beam, usually helium, and to exploit the different kinematical behaviour of the different sizes for cluster separation. By measuring their angular and velocity distributions after the scattering process in a high resolution experiment, a complete separation is achieved. This method was used by Buck and Meyer [13, 14] to size select Ar_n clusters up to $n=6$ and to measure directly the fragmentation probabilities upon electron impact ionization. The fragmentation turned out to be quite strong with the trimer totally fragmenting to dimers and monomers. Similar results were obtained for $n=4$, 5, and 6 which fragmented with a probability ratio $P(Ar_2^+)/[P(Ar_2^+)+P(Ar_3^+)]$ of larger than 0.95 to Ar_2^+. Because of experimental problems, the monomer contribution was not investigated. The first contribution to the Ar_3^+ ion came from pentamers. The dominant fragment channel was the dimer ion Ar_2^+ in spite of the fact that Ar_3^+ is the core of the larger clusters [15, 16].

After these measurements on van der Waals systems and others on ionically bound molecules [17], it was generally accepted that mass spectra of clusters do not reflect the distributions of the neutral precursors but rather the properties of the ions [18]. Exceptions are systems which do not exhibit drastic changes in structure when going from the neutral to the ionic configuration. These are, for instance, metals and aromatic molecules with delocalized electrons where the loss of one electron does not change the configuration appreciably.

Later on, the method was extended to clusters of the molecular van der Waals systems C_2H_4 [19], CO_2 [20], NO [21, 22], OCS [23], and O_2 [24]. They are all, as expected, dominated by strong fragmentation. The small closed shell molecules O_2, NO, CO_2, and also the symmetric SF_6 [8] exhibit a preference for the monomer ion. Larger molecules which consist of several atoms like C_2H_4 and OCS show a fragment pattern which is dominated by the most stable ions resulting from intracluster ion–molecule reactions. Similar results have been observed for CS_2 [25]. A special behaviour is exhibited by the hydrogen bonded systems NH_3 [26, 27], D_2O [28], N_2H_4 [23], HBr [29], and methyl lactate [30]. Here fast ion–molecule reactions [31] form protonated species which are the dominant fragment channels. Review articles

about most of these results are available [32, 33]. We note that the investigation of sodium clusters using the scattering method confirmed the expected results that the fragmentation mainly depends on the excess energy in the system [34, 35]. In this case where neutral and ionic clusters have similar structures, vertical ionization without excess energy does not lead to fragmentation.

Despite the detailed and partly surprising experimental results, theoretical calculations remained quite rare. Soler *et al.* [36] have conducted model calculation on argon, krypton, and xenon cluster ionization by assuming the initial formation of a dimer ion and following the evolution of the system by classical dynamics. This study was completed in a subsequent paper by Sáenz *et al.* [37] who showed an appreciable boiling off of argon atoms. Their results were confirmed by Stampfli [38] who studied the fragmentation of neon and xenon clusters upon ionization using classical dynamics on the ground electronic state. His results show that there is always fragmentation for the trimers. The $n = 13$ and $n = 55$ clusters also undergo strong fragmentation upon ionization. The first non-adiabatic calculation was conducted by Kuntz and Hogreve using the classical path surface hopping trajectory method [39]. This study included the lowest three adiabatic states from a diatomics-in-molecules (DIM) model of the electronic Hamiltonian, and interpreted the dissociation of the argon trimer upon ionization in terms of charge migration and non-adiabatic effects. They mainly found dimer fragments, in contrast to the experimental results where monomer ions were also observed. The first study taking into account all the potential-energy surfaces involved in the dynamics was carried out for Ar_3 and Ar_4 using a DIM model for the electronic Hamiltonian and mean-field ('hemiquantal') dynamics [40]. The results showed good agreement with experiment, both for the monomer and dimer fragment proportions and for the fact that no Ar_3^+ was observed from Ar_3 ionization and no Ar_3^+ nor Ar_4^+ from Ar_4 ionization.

A couple of years ago, Halberstadt and coworkers started a larger project for more complete simulations of the ionization and fragmentation of rare-gas clusters. All potential surfaces close to the ground state and their couplings are taken into account, and induced dipole–induced dipole interaction and spin–orbit corrections are added [41]. First results were obtained for neon clusters embedded in liquid helium droplets. The further applications of this improved theory were carried out for pure neon [42], krypton [43], and argon [44] clusters, for sizes up to $n = 14$. As a result of these simulations, a number of general features have been outlined. In agreement with experimental findings, it was shown that ionization leads to extensive fragmentation of the parent ions. In the simulation, all the rare gases (neon, argon and krypton) exhibit the same fragment pattern. Dimers are the most important fragments in the size range studied, with their proportions increasing up to a maximum and then decreasing again as a function of the neutral cluster size. The next important fragments are monomers for small initial cluster sizes and trimers, then tetramers, for larger sizes. The simulations also shed some light on the kinetics of the fragmentation, which was not possible to obtain in the experiments. They showed that fragmentation of the parent ions occurs in the picosecond time range. This is very fast compared to the average flight time of the parent ions in the detection region of a typical experiment. For the smaller cluster sizes all the dynamics is over in several tens of picoseconds.

However, for the larger sizes studied, especially for the heavier rare gases, the simulations revealed the existence of longer-lived species (100 ns or more) in a proportion that seems to be increasing with the appearance of larger stable fragments (trimers or more).

In the meantime, the measurements on Ar_n clusters were extended to $n=9$ with the monomer channels included [45]. Very recently also Kr_n was measured up to $n=7$ [46]. Thus the new and detailed calculations can directly be compared with experiment for these two systems.

It is the purpose of this article to directly confront the experimental and theoretical results on the fragmentation dynamics of rare-gas clusters upon electron-impact ionization. Rather than reviewing all the previous experimental and theoretical work on this process, we have selected the most pertinent results in this view, i.e. experiments with size selection of the neutral clusters and simulations taking into account all the relevant electronic states of the ions. Section 2 briefly recalls the principles of the theoretical modelling. Section 3 presents the neutral size selection method and the fragmentation analysis used in the experiments, and gives an overview of the experimental results on argon and krypton clusters, including the most recent ones. Section 4 is devoted to the comparison of the experimental and theoretical results for argon and krypton clusters. Following the validation of the simulation method in section 4, section 5 presents a detailed comparison of the fragmentation of neon, argon and krypton cluster upon ionization, including the kinetics of the process, a discussion of the fragmentation mechanisms, the existence of long-lived intermediate species, and the effect of spin–orbit coupling. Finally, the results are discussed in section 6 and section 7 presents conclusions and outlines perspectives for future work.

2. Theoretical modelling: a mixed quantum–classical approach

A purely quantum dynamics simulation of the fragmentation of ionized rare-gas clusters would be impossible to perform beyond the trimer due to the many degrees of freedom and the presence of a number of coupled electronic states. Because of these coupled electronic states, a purely classical treatment would not be suitable either. Mixed quantum–classical methods represent a good compromise since they can treat a large number of degrees of freedom while retaining a quantum description for one or a few crucial degrees of freedom (here the electronic states). Along the same lines, it is not feasible to determine the *ab initio* potential-energy surfaces and couplings for clusters larger than the trimer. The DIM (Diatomics In Molecules) model [15, 47–49] gives an accurate description of all the potential-energy surfaces correlating to the $Rg^+(^2P)+(n-1)$ Rg limit and their couplings for ionized rare-gas clusters.

Following these considerations, we have used the combined DIM-MDQT (Molecular Dynamics with Quantum Transitions) method to model the fragmentation of rare-gas clusters upon electron impact ionization. The MDQT method [50–52] was chosen because it is a trajectory surface hopping method, which seemed more natural for fragmenting systems. Other works [40], including very recent ones [53–55], use mean-field methods, although so far only results for small cluster sizes have been published. It would be very interesting to compare the results of the two different types of methods

for an extensive range of sizes. The present DIM-MDQT method has been described in details elsewhere [41–44] and we only recall here some essential features.

The DIM model uses the Rg_2^+ and Rg_2 potential curves to build the electronic Hamiltonian matrix for Rg_n^+. It is particularly simple in the case of Rg_n^+ since the Hamiltonian matrix can be expressed in the basis set of p orbitals for the (single) electronic hole. Analytical forms for Rg_2 curves were taken from the literature [56, 57] whereas analytical forms for Rg_2^+ curves have been fitted on *ab initio* calculations from Ha *et al*. [58]. This traditional DIM model has been improved by including the induced dipole–induced dipole interaction [59] and the spin–orbit (SO) coupling [58–60].

In our application of the MDQT method the nuclei are treated classically and electrons (here the electronic hole) quantum mechanically. The nuclei evolve on one adiabatic potential-energy surface at a time. The multisurface character of the problem is taken into account by allowing for hops between surfaces, with hopping probabilities governed by the time evolution of electronic state probabilities during the electronic wave packet propagation. At a hopping event the sudden change in potential energy imposes an adjustment of atomic momenta in order to conserve total energy. Determining how this energy is dispatched among the atomic momenta amounts to selecting a vector in the $3n$ space along which momenta are adjusted. The choice of such a vector remains arbitrary although some justifications have been offered for some specific choices [61, 62]. We have used the gradient of the potential energy difference between the surfaces involved in the hop, namely $\nabla(V_k - V_j)$ for a hop from state j to state k. A detailed discussion on the choice of this hopping vector can be found in [42].

Initial conditions for the trajectories are designed to reproduce the experimental conditions as closely as possible. The neutral clusters are formed in a supersonic expansion and are therefore assumed to be in their ground vibrational state. Electron-impact ionization performed with $\sim$70 eV electrons is very fast (less than a femtosecond) compared to any nuclear motion. Therefore it is assumed to be 'vertical', i.e. instantaneous and for fixed positions of the nuclei. The excess energy is assumed to be shared between the ionizing and the other departing electron, so that the momenta (velocities) of the nuclei are also unchanged. Since the energy width associated with subfemtosecond excitation is of several eV, 70 eV ionization is assimilated to coherent white light excitation. These experimental conditions are translated in the simulation as follows. A classical trajectory is run for the neutral cluster at a total energy equal to its zero-point energy. After some time for energy randomization, vertical ionization is performed at regular time intervals. A new trajectory is started for the parent ion, with initial positions and momenta of the nuclei equal to those in the neutral cluster at the time of ionization and a randomly selected electronic state for the classical propagation. The equivalence of all the electronic states is mirrored in the initial condition for the electronic quantum wave packet by equal coefficients for all the states. We have checked that starting the wave packet propagation from a randomly chosen pure adiabatic electronic state does not affect the final fragment proportions. Note however that fragmentation strongly depends on the initial electronic state as will be discussed later, so that for a different ionization process that would selectively ionize one of the electronic states of the parent ion the results would be different [43, 44, 63].

3. Experiments

3.1 *Size selection*

As described in detail in earlier publications [14, 32, 33], the scattering analysis of a cluster beam enables us to find a unique correlation between detected cluster ions and their neutral precursors, independent of the cluster size distribution in the primary beam and the fragmentation process taking place in the ion source. The method relies on the specific kinematic behaviour of clusters with different sizes scattered from a target beam and is commonly described in terms of a velocity vector diagram as shown in figure 1. Because of the scattering process of the rare-gas clusters with the light helium target atoms, each cluster with a certain size can be scattered into the laboratory (lab) system only within a certain angular range. This is visualized in figure 1 by the different circles representing the final centre-of-mass (cm) velocities of elastically scattered clusters. The largest circle represents the scattering of the monomer, whereas the smaller circles define the corresponding values for the cluster scattering up to the tetramer. The scattering process implies that for each cluster size n a corresponding specific maximum scattering angle $\theta_{\max}(n)$ exists. Thus the selection of a specific detection angle in the lab system is acting as a 'low pass filter'. All larger rare-gas clusters with $n > n_{\max}(\theta)$ are excluded from being detected, since they have smaller maximum scattering angles. At the laboratory scattering angle θ depicted in figure 1 only the cluster sizes $n = 1, 2, 3$ are detected.

Under typical experimental conditions with moderate energy transfer during the scattering process, clusters of different sizes that are scattered in one lab angle θ arrive with different velocities. This is shown pictorially in the right panel of figure 1 which displays the intensity contributions along the final velocity. This behaviour allows us to disentangle the various cluster contributions measured at the mass of the monomer. In order to get this information, velocity resolved measurements of the scattered particles are necessary. The intensity of the scattered neutral cluster of size

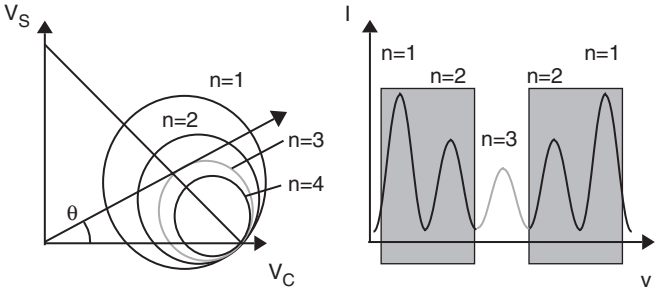

Figure 1. Schematic velocity vector diagram for the scattering of a cluster by an atomic beam. The cluster $n = 3$ is selected by angular (left panel) and velocity (right panel) selection. $\mathbf{V_C}$ and $\mathbf{V_S}$ respectively denote the cluster and the helium scattering beam velocities in the laboratory frame. The velocity $\mathbf{V_{G_n}}$ of the He–Rg$_n$ centre of mass G_n is constant. For elastic scattering, the modulus of the relative velocity $\mathbf{V_n} = \mathbf{V_C} - \mathbf{V_S}$ is conserved, hence the end of the cluster velocity vector in the lab frame after collision $\mathbf{V'_C} = \mathbf{V_{G_n}} + [m_s(m_s + m_C)]/\mathbf{V'_n}$ describes a circle centred on G_n and with radius $[m_s(m_s + m_C)]/\mathbf{V_n}|$.

n, at the laboratory angle θ, final velocity v', and detected at the mass k of the mass spectrometer is given by

$$N_{nk}(\theta, v') = K\rho_n\sigma_n C_n f_{nk}. \tag{1}$$

The constant K contains the variables concerning the scattering process which are not relevant for the cluster separation, ρ_n is the cluster density, σ_n is the differential scattering cross-section with the helium scattering beam in the lab system, C_n is the total ionization cross-section, f_{nk} is the probability for the formation of an ion of mass k from a cluster of size n with $\Sigma_k f_{nk} = 1$. Here the signals are already corrected for different transmissions of the mass filter. If no velocity analysis is applied, the signal $S_k(\theta)$ is summed over all neutral cluster sizes which may contribute at this scattering angle to the fragment mass k

$$S_k(\theta) = \sum_{n=k}^{n_{\max}(\theta)} N_{nk}. \tag{2}$$

This clearly illustrates that in the case of fragmentation during the ionization process, N_{nk} ionic fragments can be detected at the selected ion mass k from neutral clusters with sizes n up to $n = n_{\max}(\theta)$.

3.2 *Fragmentation analysis*

Using the definition of equation (1) and the relation $\Sigma_k f_{nk} = 1$, the fragmentation probabilities f_{nk} are given by

$$f_{nk} = N_{nk} \Big/ \sum_{k=1}^{n} N_{nk}. \tag{3}$$

To determine the fragmentation probabilities f_{nk} experimentally, it is necessary to measure the intensities $N_{nk}(\theta, v')$ at the specified deflection angle θ and the final velocity v'. There are two different ways to carry out these measurements. We will briefly discuss them.

1. The easiest way to do this is to determine the velocity using a selector after the collision has taken place. The detector is placed at a selected angle and the velocity selector transmits only a certain velocity range. This is shown pictorially at the right hand side of figure 1 for $n = 3$ in which the shaded area is blocked and the bright area is passed by the selector. In this way, n is completely specified and the intensities at the different fragment masses k measured by the mass spectrometer give directly the fragmentation probabilities. Such an arrangement has been used in the improved experiment on Ar_n clusters [45].
2. If, in contrast, the velocity is measured by time-of-flight (TOF) techniques, we only know after the analysis which neutral cluster size belongs to which fragment mass. What is mainly measured in a TOF distribution are the

amount of different n at one k. For the fragmentation probabilities f_{nk} one needs different k for one n. Therefore one has to relate the measurements at different k to each other. In the original paper by Buck and Meyer the intensities $N_{nk}(\theta, v')$ were directly compared with each other [14]. This is the way in which the results for the argon dimers and trimers have been obtained. Later on, it turned out [27] that it is more convenient and accurate to use only the relative intensities of the TOF distributions X_{nk} given by

$$X_{nk}(\theta) = N_{nk} \Big/ \sum_{n=k}^{n_{\max}(\theta)} N_{nk}, \tag{4}$$

and to relate them to the measured total scattered intensity $S_k(\theta)$. By combining equations (2) and (4) with equation (3) we get the probability f_{nk} for a neutral cluster of size n to fragment into an ion with mass k

$$f_{nk} = S_k X_{nk} \Big/ \sum_{k=1}^{n} S_k X_{nk}. \tag{5}$$

Here f_{nk} is expressed by two easily measurable quantities, S_k, obtained from the differential cross-section measurements, and X_{nk}, obtained from the analysis of time-of-flight measurements of the scattered beam. This is the way in which the results for the krypton clusters have been obtained [46].

3.3 *Results*

The results of the fragmentation analysis for Ar_n and Kr_n clusters which are presented in this article are obtained in two different crossed molecular beams apparatus. They both consist of two supersonic nozzle beams which are generated in two differentially pumped source chambers and which are crossed at an angle of 90° in the scattering centre. For angular dependent measurements, the complete base of the scattering chamber is rotated with respect to the scattering centre, while the detector position is fixed. The detector consists of a time-of-flight (TOF) spectrometer, using the pseudorandom chopping technique, and a mass spectrometer consisting of an electron bombardment ionizer and a quadrupole mass filter. The electron beam was operated at an energy of 70 eV. The first apparatus, called (A), has higher resolution in angle and velocity [64]. The second apparatus, called (B), allows us to implement a velocity selector after the scattering centre [29, 45]. For the details of the cluster production, the geometrical dimensions, and the data evaluation procedures, we refer to the original articles. We will indicate the data set by the apparatus in which they are obtained, (A) or (B), and the method which has been used in the fragmentation analysis, (1) with a velocity selector or (2) with TOF analysis, presented in the previous subsection.

The experimental results of the fragmentation probabilities for the Ar_n and Kr_n clusters are presented in tables 1 and 2. Argon was detected at $m/z = 40$ u and the corresponding multiples. For krypton $m/z = 84$ u was chosen as the basis mass unit. The results for Ar_n were obtained by procedure (A,2) for $n = 2$ and 3, and for the rest by procedure (B,1). For Ar_n from $n = 2$ to $n = 9$ the dominant channel is, with the exception of $n = 4$, the dimer ion Ar_2^+. The remarkable fact is that for $n = 4$ and

Table 1. Fragmentation probabilities f_{nk} of the cluster size n to the ion size k for argon. The data are obtained by method (A,2) [14] ($n = 2, 3$) and method (B,1) [45] ($n = 4$–9).

n	$k = 1$	$k = 2$	$k = 3$
2	0.40	0.60	–
3	0.30	0.70	0.00
4	0.56	0.44	0.00
5	0.29	0.67	0.04
6	0.42	0.54	0.04
7	0.22	0.71	0.07
8	0.22	0.73	0.05
9	0.34	0.51	0.15

Table 2. Fragmentation probabilities f_{nk} of the cluster size n to the ion size k for krypton. The data are obtained by method (A,2) [46].

n	$k = 1$	$k = 2$	$k = 3$
2	0.951	0.049	–
3	0.973	0.027	–
4	0.961	0.039	–
5	0.965	0.029	0.006
6	0.926	0.053	0.021
7	0.902	0.063	0.035

$n = 3$ no intensity was observed at other masses than those of dimer and monomer, the parent masses included. These results agree with the tendency observed in the previous measurement (A,2) [14] of the dimer ion channel which gave the relative probabilities $f_{n2}/\sum_{k\geq 2} f_{nk}$ 1.00 for $n = 4$, 0.98 for $n = 5$, and 0.95 for $n = 6$. Note that in this experiment the numbers refer to the dimer or larger products, since the monomer channel Ar^+ was not measured. The results of the experiments (B,1) are 1.00, 0.94, and 0.93 for the same probabilities.

In contrast, the main fragmentation channel of Kr_n clusters is the monomer ion Kr^+ with a probability larger than 0.9 for $n = 2$ to $n = 7$. The probability of observing dimer ions Kr_2^+ is much smaller than expected for each initial cluster size. The trimer ion Kr_3^+ appears first from the neutral Kr_5, and its fraction increases with increasing neutral cluster size n, but is always much smaller than that of the monomer or dimer. This experiment was carried out with method (A,2). In an early stage of the experiment the other apparatus (B,2) was used and the results agreed within experimental errors. As an example of a typical measurement we present the angular dependent distributions $S_k(\theta)$ for krypton, measured at the seven fragment masses k [46]. The results are shown in figure 2. The shaded areas mark the theoretical limiting scattering angles θ_n for the neutral cluster n, broadened by the finite resolution of the apparatus. In general, the dominating fragment is the monomer ion (black). The onset of the dimer ion intensity (red) is in good agreement with the predicted limiting angle. The first contribution of the trimer ion (green) comes from the neutral pentamer. Fragment ions larger than the trimer ion are detected but contribute less than 1% of the total intensity for neutral Kr_n clusters up to $n = 7$.

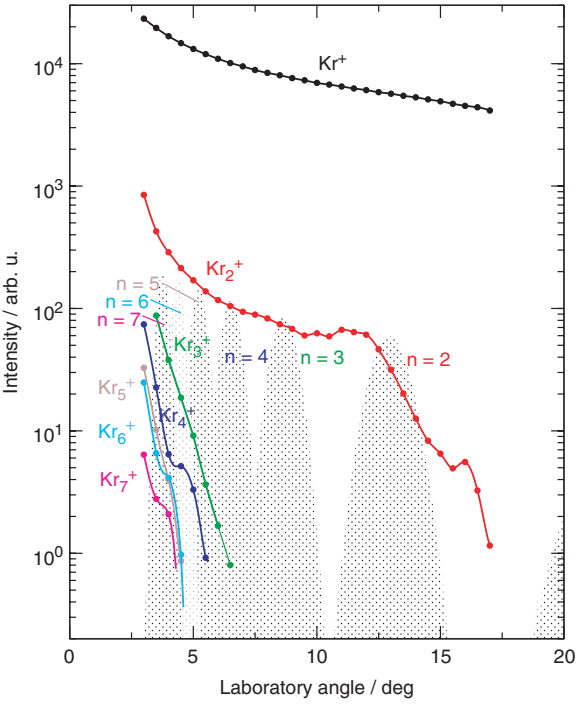

Figure 2. Measured angular dependence of scattered krypton clusters $S_k(\theta)$ at the masses k indicated [46]. The shaded areas mark the onset of the different neutral cluster sizes n.

Although the final fragmentation probability in method (A,2) is obtained from the additional measurement of the relative intensity X_{nk} of a TOF distribution (see equation (5)), these values have to be multiplied by the total intensities S_k. Based on the measurement of figure 2, it is obvious that the values of the monomer intensity S_1 is two orders of magnitude larger than that of the dimer fragment S_2. These results demonstrate pictorially the final result of krypton clusters which is dominated by monomer fragments.

The results for krypton were quite surprising to us, and that is why we repeated the initial experiments (B,2) on the second scattering machine that yields more precise results (A,2). As a cross check the total angular distributions of argon clusters were measured in apparatus (B) [65]. The result for the monomer and dimer fragments is given in figure 3. Now the dimer fragment intensity S_2 is only one order of magnitude less than that of the monomer fragment intensity S_1. This explains the large difference with the krypton result and is a further experimental confirmation of the different behaviour of the two systems.

4. Comparison between theory and experiment for Ar_n and Kr_n

The method described in section 2 provides a complete description of the rare-gas cluster dynamics following ionization, including non-adiabatic and spin–orbit effects.

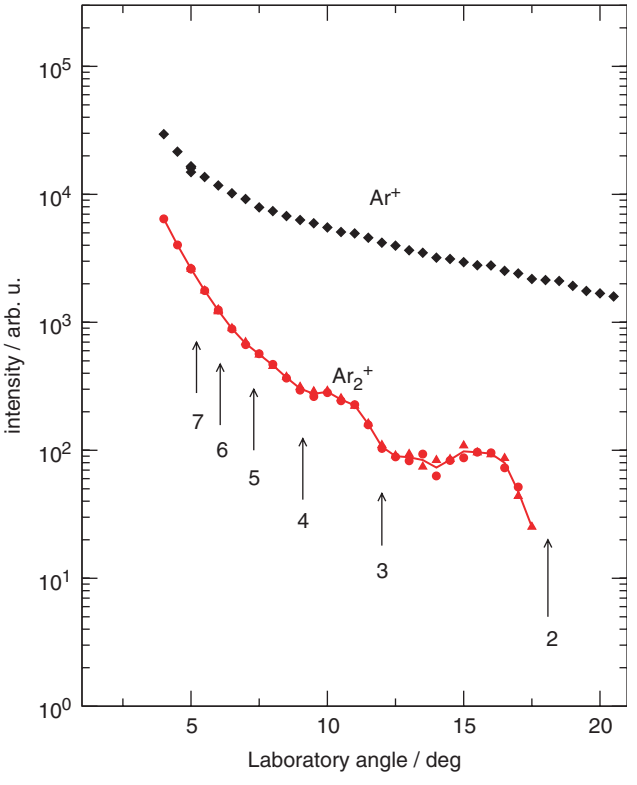

Figure 3. Measured angular dependence of scattered argon clusters $S_k(\theta)$ at the masses k indicated [65].

In particular, the final fragment distributions can be determined and compared with experiment. Experiments like the ones pioneered by Buck and Meyer [13, 14, 32] and described in section 3, in which the clusters are size-selected prior to ionization, are particularly meaningful in this context: a direct comparison can be performed without any need for averaging over an initial neutral cluster size distribution.

4.1 *Fragmentation of the $(Ar_n^+)^*$ parent ions*

Figure 4 presents the simulated results of Bonhommeau *et al.* [44] for the sum of the Ar^+ and Ar_2^+ fragment proportions as a function of initial cluster size n, $n = 2$–11, compared with the experimental results of Buck and Meyer [14] and Lohbrandt *et al.* [45] for $n = 2$–9. The experimental and theoretical results are in very good agreement. In particular, they reveal very extensive fragmentation of the parent ions: the Ar^+ and Ar_2^+ final proportions sum up to almost 100% for $n \leq 6$. They decrease monotonically with parent ion size for $6 \leq n \leq 11$ but they still represent more than 65% of detected fragments for $n = 11$.

However, a more careful examination of the experimental and theoretical results reveals some differences. Figure 5 presents the Ar^+, Ar_2^+, Ar_3^+, and Ar_4^+ fragment abundances originating from the fragmentation of $(Ar_n^+)^*$ clusters ($n = 2$–11). The agreement

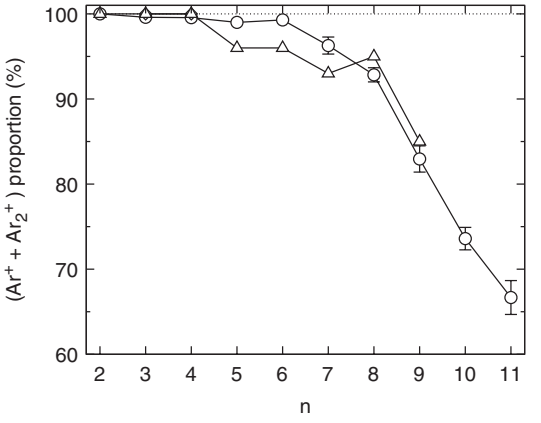

Figure 4. Sum of the Ar^+ and Ar_2^+ proportions (%) following electron-impact ionization of Ar_n for $n = 2$–11. Comparison between the simulated results (circles) of Bonhommeau *et al.* [44] and the experimental results from Buck and Meyer [14], for $n = 2$, 3, and from Lohbrandt *et al.* [45], for $n = 4$–9 (upward triangles). Simulated results correspond to 100 ps propagation, involving SO couplings up to $n = 9$, and neglecting it for $n = 10$ and $n = 11$. Reproduced from [44], figure 1, with permission.

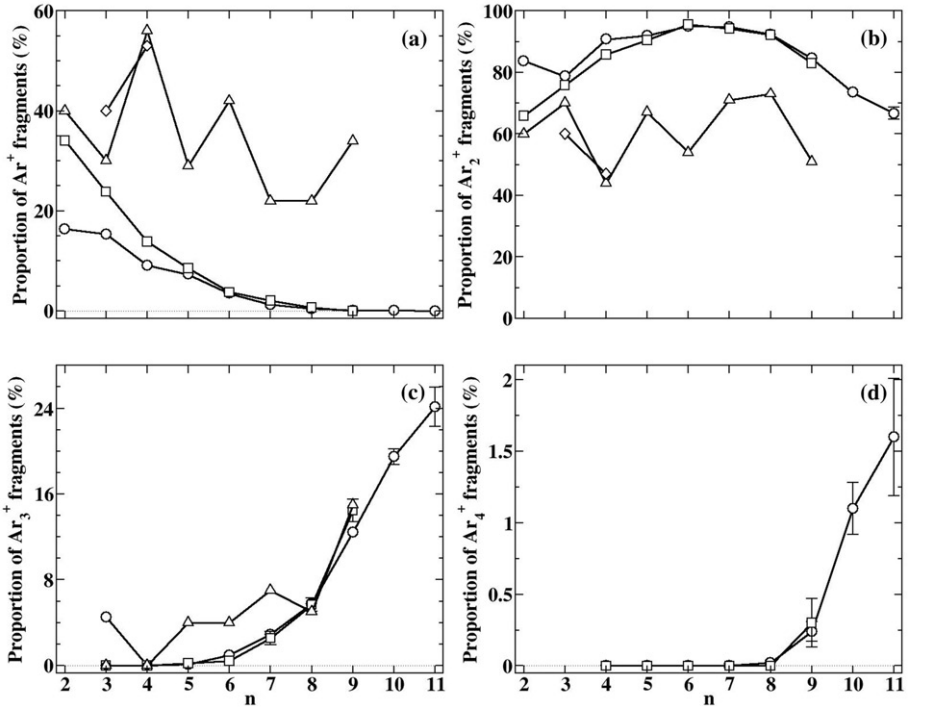

Figure 5. Proportions (%) of (a) Ar^+, (b) Ar_2^+, (c) Ar_3^+ and (d) Ar_4^+ fragments as a function of the initial cluster size. The simulation results [44] including (squares) or neglecting (circles) the SO interaction are compared to available experimental data from Buck and Meyer [14], for $n = 2$, 3, and from Lohbrandt *et al.* [14], for $n = 4$–9 (upward triangles). They are also compared to the simulation results of Bastida *et al.* [40] (diamonds). The statistical uncertainty is only specified when it exceeds the size of the plotting symbols. Reproduced from [44], figure 2, with permission.

is very satisfactory for the larger Ar_p^+ ($p = 3$–4) fragments: Ar_3^+ fragments start appearing for $n \leq 5$, their abundance monotonically increasing with the parent ion size, and no Ar_4^+ fragment is produced for $n < 9$. Moreover, Ar_2^+ are the most abundant fragments for all initial cluster sizes, which also agrees with experimental results by Lohbrandt *et al.* [45] (except for $n = 4$). However, the individual theoretical proportions of Ar^+ and Ar_2^+ do not fit the experimental results. The theoretical modelling predicts a systematic and monotonic evolution of Ar^+ and Ar_2^+ proportions. The monomer abundance decreases from 34% for $n = 2$ to zero for $n = 9$ and the dimer abundance increases from 66% for $n = 2$ to a maximum value of 95% for $n = 6$ before decreasing down to 67% for $n = 11$. Experimental proportions are in good agreement with the theoretical ones for $n = 2$–3, but then begin to oscillate for $n \leq 4$ with a slight tendency to decrease for ionic monomers and no significant tendency for dimers. Moreover, the experimental abundance in dimers (resp. monomers) is smaller (resp. larger) than the theoretical one for a given parent ion size.

Figures 5(a) and 5(b) also present the theoretical results obtained by Bastida *et al.* [40] for $n = 3$–4. Their simulation uses the same kind of potential-energy surfaces (without including the SO interaction) as in our method, and a different approach to model the dynamics of the ionized argon clusters, namely the mean-field approach. Their results are very close to the experimental ones, but it cannot be checked whether they would reproduce the experimental oscillations since they were restricted to $n = 3$–4. A recent study [54] limited to the trimer and using the same approach gives 24% and 27% of Ar^+ fragments without and with SO interaction, respectively, which is closer to our results. The difference with the results of Bastida *et al.* must originate from different input potential curves. We also note that including the SO interaction would certainly alter the fragment abundances obtained by Bastida *et al.* This interaction has a significant effect on small clusters, as can be seen in figure 5: the Ar^+ abundance is doubled when the SO interaction is taken into account in the dynamics of $(Ar_2^+)^*$. Inclusion of the SO interaction in the $(Ar_3^+)^*$ dynamics increases the Ar^+ fragment proportion by about 30%. It also suppresses the production of Ar_3^+, which originated from the existence of a potential well in the neutral trimer Franck–Condon region for one of the $(Ar_3^+)^*$ electronic states. However, the SO interaction does not change the theoretical results for $n \geq 6$, which justifies neglecting it for larger clusters ($n \geq 10$).

4.2 *Fragmentation of the $(Kr_n^+)^*$ parent ions*

We now turn to the comparison of the results of the calculations [43] with the experiments introduced and discussed in section 3 [46] for krypton clusters. As discussed in [46], both theory and experiment reveal extensive fragmentation and they agree on the minimum parent ion size for the appearance of the trimer ion channel. This is demonstrated in figure 6, where the fragmentation probabilities for the trimer ion f_{n3} and the sum of that for the monomer and the dimer ion $f_{n1} + f_{n2}$ are plotted as a function of the initial cluster size n. The figure also contains the results without spin–orbit interaction. While the results for the larger clusters do not differ very much from those with spin–orbit interaction included, there is a pronounced difference for the trimer. An appreciable fraction of Kr_3^+ originates from the existence of a minimum in one

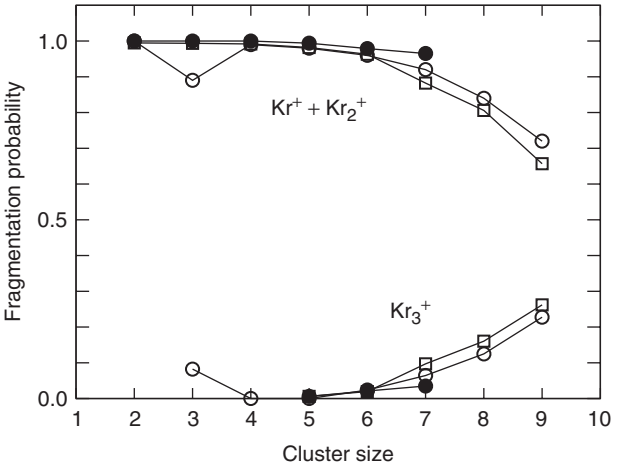

Figure 6. Comparison of measured [46] and calculated [43] fragmentation probabilities of $f_{n1} + f_{n2}$ and f_{n3} for Kr_n, $n = 2$–9. Experiment: closed symbols, calculation: open symbols, circles without and squares with spin–orbit interactions.

of the electronic states close to the equilibrium configuration of neutral Kr_3, which disappears when the spin–orbit interaction is included [43] in agreement with experiment.

However, if we look at the direct comparison of the fragmentation probabilities f_{n1} and f_{n2} into the monomer and the dimer ion channels, the agreement is less good. There is a qualitative agreement in the sense that the abundance in Kr^+ decreases while the abundances in Kr_2^+ and Kr_3^+ increase with parent ion size. On the other hand, the calculations predict that 50% of the dimers fragment to Kr^+ monomers upon ionization, and this fraction drops rapidly with increasing neutral cluster size. For $n > 4$, the calculated probability of observing the Kr^+ monomer ion is always less than 20%, whereas the experimental value remains close to 90% up to $n = 7$, the largest neutral size studied. Similar discrepancies occur for the fragmentation probabilities f_{n2} to the dimer ion. Here the calculated values increase from 49% for $n = 2$ to a maximum at 84% for $n = 6$ and then drop again to 63% for $n = 9$, while the experimental values oscillate between 2.7% and 6.3%. There is good agreement between experiment and theory as for the strong fragmentation into monomer and dimers ions, but the main disagreement is specifically the branching ratio between monomer and dimer ions.

We note that including the spin–orbit interaction in the calculation significantly increases the fragmentation to the Kr^+ monomer for $n = 2$ and 3. This effect is masked in figure 6 by the simultaneous decrease of the fragmentation probability to dimer ions. Given that the effects of spin–orbit excitation double the calculated probability of obtaining Kr^+ monomer ions from ionization of the neutral dimer, it may be worth further exploring the details of the excitation cross-sections to spin–orbit excited states to improve the agreement between experiment and theory.

4.3 *Secondary ionization of neutral fragments*

The partial disagreement of the experimental and theoretical results can have very diverse origins. On the one hand, the calculations might have neglected contributions which turned out to be important. On the other hand, the experimental results might not be exactly what is calculated. A possible contribution to this latter case is the fact that in the ion source neutral fragments which originate from the fragmentation process are ionized and increase the corresponding signal. The calculations demonstrate that for each neutral cluster size, aside from the ionic fragments, also about $n-2$ neutral monomer fragments are generated. Provided that these fragment atoms are also ionized by the electrons of the ion source, the intensity of the monomer ions will increase appreciably. This correction is simple in the case of the Ar_n clusters, since the main results have been obtained by the velocity selector method (1). We have evaluated this correction by assuming that all neutral monomers are ionized. The result is displayed in figure 7. The agreement is much better: the qualitative behaviour of the theoretical and experimental curves is the same and the oscillations are damped; the quantitative behaviour is also very satisfactory for all cluster sizes. Analysis of the simulations also revealed that the fragmentation dynamics occur on the picosecond time scale (see section 5.1.1) and that the vast majority of neutral fragments are monomers. Given the microsecond flight time of the clusters in the ionization region, it is thus plausible that neutral monomer fragments are ionized which tends to confirm our hypothesis.

The case of the krypton clusters is more complicated. The main difference is that already the result for the dimer, which agreed in the argon case, exhibits

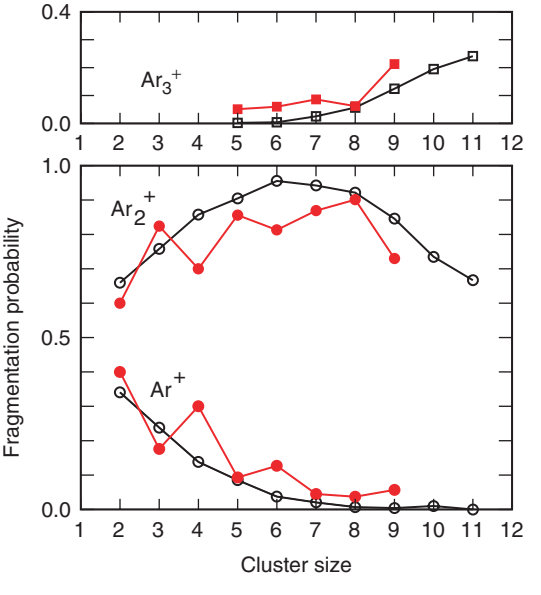

Figure 7. Comparison of measured [14, 45] and calculated [44] fragmentation probabilities for Ar_n, $n=2$–11. Experiment, corrected for secondary ionization of monomer fragments: closed symbols; calculations: open symbols.

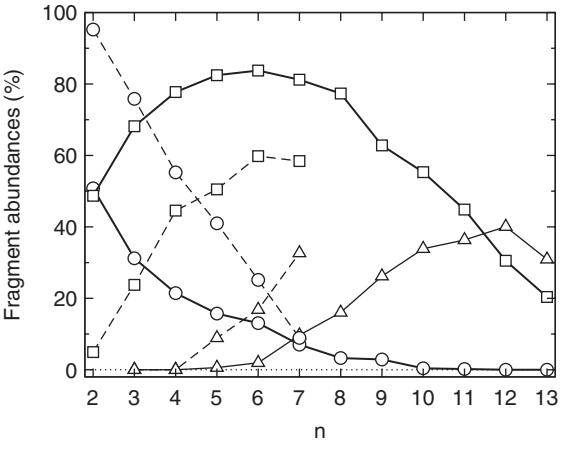

Figure 8. Theoretical (solid curves) and experimental (dashed curves) [46] fragment abundances (%) as a function of the initial cluster size ($n = 2$–13): Kr^+ (circles), Kr_2^+ (squares) and Kr_3^+ (upward triangles). The experimental results are corrected for secondary ionization of neutral monomer fragments. The theoretical results are derived from [43] for $n \leq 11$ and unpublished results for $n = 12$ and $n = 13$.

large discrepancies. Since we do not expect any corrections of the secondary ionization for the dimer, the main reason for the general discrepancy should be a different one. Nevertheless we applied this correction also to the krypton clusters. In this case the TOF method (2) was used in the experiment. Here both the total intensities S_1 and the X_{n1} values of the time-of-flight distributions are affected and have to be corrected. A tentative correction of this effect was carried out and compared with theoretical results for $n \leq 11$ and new calculations for larger cluster sizes. The results are presented in figure 8. This correction leads indeed to a drastic decrease of the monomer ion contribution, especially for the larger clusters. The qualitative behaviour of the experimental and theoretical curves for $n \leq 7$, which is the largest size experimentally investigated, is similar. The abundance of Kr^+ decreases while the amount of Kr_2^+ and Kr_3^+ increases with growing parent size. But the deviations in absolute values are still large. Note that Janeček *et al.* [54] also obtain a small proportion of Kr^+ fragments (24%) in their DIM + mean field study of Kr_3 ionization. It appears that if the discrepancy which already occurs for the dimer parent ion is understood and removed, the agreement in all three channels would be appreciably improved.

5. Theoretical comparison of the $(Ne_n^+)^*$, $(Ar_n^+)^*$ and $(Kr_n^+)^*$ fragmentation

The comparison with experiment has validated the results of the simulation. In particular, extensive fragmentation of parent ions is found with no trimer fragment for $n < 5$. We can now turn to a more detailed analysis of the results of the simulation, which can be extended not only to cluster sizes $n > 9$ but also to other rare-gas clusters like the neon ones which have not yet been experimentally studied. We compare in this section the theoretical results obtained for neon, argon and krypton clusters ($n = 2$–14). Unless

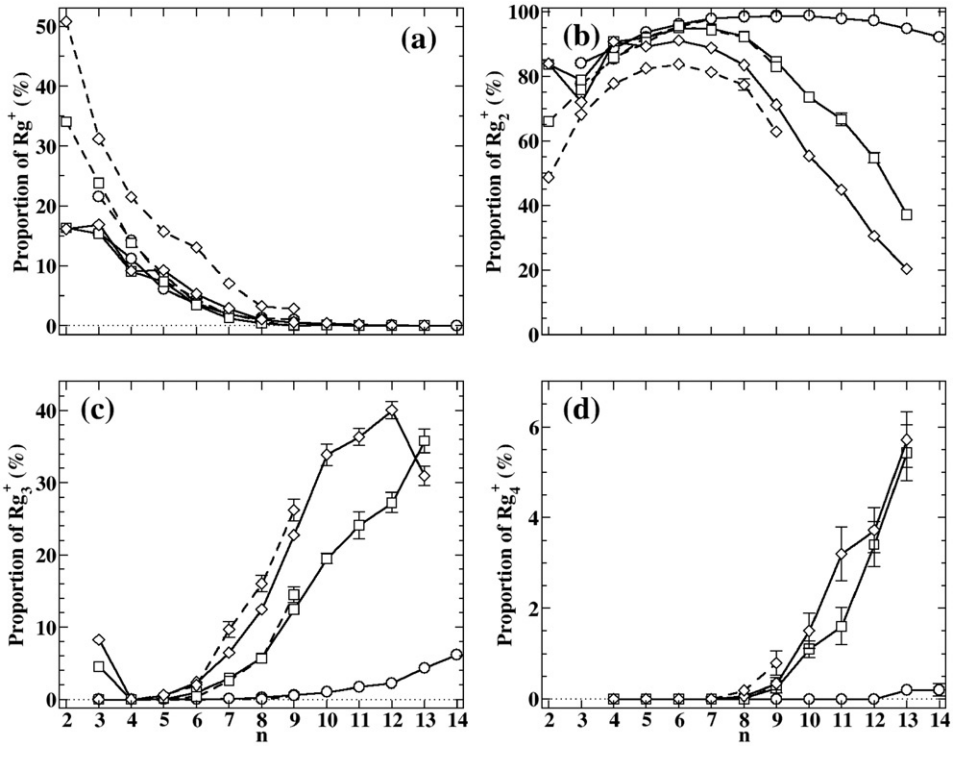

Figure 9. Theoretical abundance (%) of the (a) Rg^+, (b) Rg_2^+, (c) Rg_3^+ and (d) Rg_4^+ fragments following electron-impact ionization of neon (circles), argon (squares) and krypton (diamonds) clusters, as a function of the initial cluster size ($n = 2$–14). These results are obtained from a 100 ps mixed quantum–classical propagation, neglecting (solid curves) or including (dashed curves) the SO interaction. Statistical uncertainties are only specified when they exceed the size of the plotting symbols.

otherwise specified, the symbol Rg will refer to all the studied clusters, i.e. neon (Ne), argon (Ar) and krypton (Kr) clusters.

Figure 9 presents the Rg^+, Rg_2^+, Rg_3^+ and Rg_4^+ fragment abundances following electron-impact ionization of Rg_n clusters ($n = 2$–14). Larger Rg_p^+ ($p \geq 5$) fragments are also produced but their contribution never exceeds 1–2% for all the neutral cluster sizes examined here. For instance, the fragmentation of $(Ar_{13}^+)^*$ leads to $2.0 \pm 0.5\%$ of Ar_5^+ and the fragmentation of $(Kr_{13}^+)^*$ leads to $1.4 \pm 0.4\%$ of Kr_5^+ and some larger fragments. The present work is focused on the smaller ionic fragments ($n \leq 4$).

The results presented in figure 9 demonstrate that the fragmentation of ionized rare-gas clusters is extensive for all rare gases: the size of the fragments is much smaller than that of the parent ions. Figure 9(b) also reveals that Rg_2^+ are the most abundant fragments in most cases. $(Ar_{13}^+)^*$, $(Kr_{12}^+)^*$ and $(Kr_{13}^+)^*$ are the only parent ions whose fragmentation preferentially leads to the ionic trimer rather than to the ionic dimer (see figure 9(b) and figure 9(c)).

The fragment proportion curves exhibit the same trends for all the rare gases. The proportion of Rg^+ steadily decreases to zero (or almost zero) for $n = 9$ (see figure 9(a)). The proportion of Rg_2^+ starts increasing, reaches a maximum ($n = 9$

for neon clusters and $n=6$ for argon and krypton clusters), and then decreases (see figure 9(b)). Moreover, the increase in neutral cluster size leads to the stabilization of larger fragments. The proportions of Rg_3^+ and Rg_4^+ monotonically grow with parent ion size, except for the particular case of $(Kr_{13}^+)^*$ (see figure 9(c) and figure 9(d)), which might indicate that Kr_3^+ proportion has reached its maximum for $n=12$. The proportion of trimer fragment ions starts being significant ($\geq 0.5\%$) for $n=9$, 6 and 5 for neon, argon and krypton clusters, respectively. Heavier rare gases tend to give larger fragments, the main difference being between neon and the other rare gases (krypton and argon). This propensity can be accounted for by considering the relative binding energies of the rare-gas clusters. Although the Kr_2^+ potential energy well ($De(Kr_2^+)=11006\,cm^{-1}$) is shallower than the Ar_2^+ one ($De(Ar_2^+)=11236\,cm^{-1}$), which is itself shallower than the Ne_2^+ one ($De(Ne_2^+)=12162\,cm^{-1}$) [42–44, 58], the dissociation energy of additional atoms is in the reverse order, certainly because of the larger polarizability of the heavier rare gases. Since the fragmentation process occurs most often by the loss of neutral monomers, it relaxes more energy at each step for the heavier rare gases, therefore leading to larger final fragments.

5.1 *Characteristic times of the dynamics*

In this section we present characteristic times of the fragmentation dynamics following electron-impact ionization of neon, argon and krypton clusters obtained from the simulation. In addition to characterizing the fragmentation dynamics, these predicted times give indications on the mechanism of the process. An experimental determination would be very interesting in order to confirm the validity of the predictions.

Figure 10 presents the time evolution of intermediate-species abundances during the fragmentation process of $(Ne_9^+)^*$, $(Ar_9^+)^*$ and $(Kr_9^+)^*$. The fragmentation is clearly sequential: the octamer peak occurs before the heptamer peak, which occurs before the hexamer peak, etc. until obtaining stable fragments, i.e. mainly Ne_2^+ for neon clusters, Rg_2^+ and Rg_3^+ for argon and krypton clusters. This result is general for all the studied cluster sizes. Although final fragment proportions are nearly converged after 10 ps in the case of neon clusters, it takes much more time for argon and krypton clusters to reach convergence. This will be discussed in section 5.1.2. However, all the parent ions fragment rapidly. Section 5.1.1 presents their lifetimes and analyses the factors governing them. It is seen that the evolution with parent ion size is not always monotonic. A new theoretical interpretation is presented, showing that this modulation can be related to the equilibrium configuration symmetry of the initial neutral cluster, and that the importance of this modulation depends on the zero-point energy.

5.1.1 Parent ion lifetimes. The lifetimes of the parent ions are determined by fitting their disappearance curves (like those presented in figure 10 for ionic nonamers) to a simple analytical exponential form

$$f(t) = 100 \exp\left[\frac{-(t-t_0)}{\tau}\right] \tag{6}$$

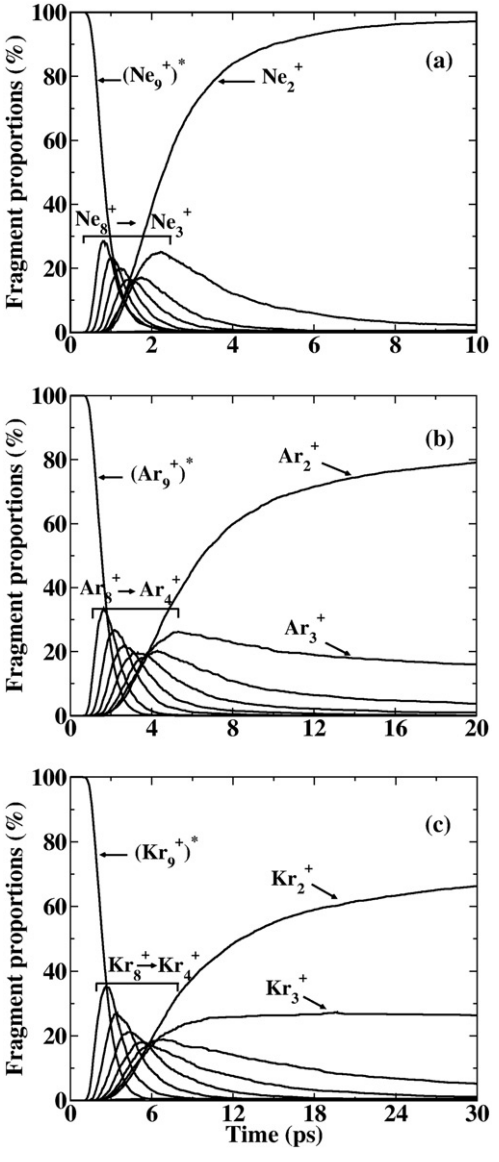

Figure 10. Time-dependent evolution of intermediate-species abundances during the fragmentation process of (a) $(Ne_9^+)^*$, (b) $(Ar_9^+)^*$ and (c) $(Kr_9^+)^*$. (The SO interaction is not included.) Plot (a) is reproduced from [42], figure 7, and plot (c) from [43], figure 4, with permission.

where τ is the parent ion lifetime and t_0 the time delay for the first atoms to reach the fragmentation distance (fixed to 8, 11 and 11.5 Å for neon [42], argon [44] and krypton [43] clusters respectively).

The resulting parent ion lifetimes are presented in figure 11. They become longer as the rare-gas mass increases. The fragmentation of the argon parent ions is about 1.5 to 2 times slower than for neon clusters and 1.3 to 2.3 times faster than for krypton clusters.

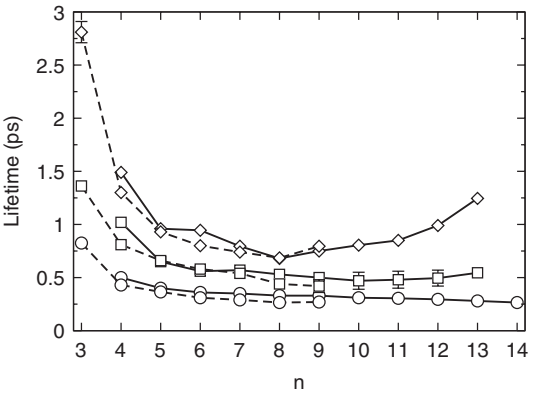

Figure 11. Parent ion lifetimes of $(Ne_n^+)^*$ (circles), $(Ar_n^+)^*$ (squares) and $(Kr_n^+)^*$ (diamonds) as a function of their size ($3 \leq n \leq 14$). Lifetimes when neglecting (solid curves) or including (dashed curves) the SO interaction are both presented. Statistical uncertainties are only specified when they exceed the size of plotting symbols. No lifetime was determined for trimers in the calculations that neglect spin–orbit couplings since the coexistence of the two A′ and A″ symmetry classes would have required the determination of a lifetime for each of them.

Moreover, the $(Ne_n^+)^*$ lifetime decreases monotonically with increasing parent ion size. Adding one atom to a cluster increases by 3 the number of coupled electronic states, which accelerates electronic relaxation and leads to faster fragmentation. However, for argon and krypton clusters the lifetime decreases down to a minimum for $n = 10$ and $n = 8$ respectively, but with some singular points, and $n = 13$ is a clear maximum for krypton.

To understand the origin of this effect, first note that $(Kr_4^+)^*$, $(Kr_6^+)^*$, $(Kr_8^+)^*$ and $(Kr_{13}^+)^*$ are special points on the parent ion lifetime curve in figure 11: $(Kr_4^+)^*$ is the first maximum of the curve, $(Kr_6^+)^*$ is a local maximum, $(Kr_8^+)^*$ corresponds to the minimum of the curve and $(Kr_{13}^+)^*$ is a second maximum. A longer lifetime indicates a smaller number of coupled electronic states at the beginning of the dynamics. Because the zero-point energy (ZPE) is very small for neutral krypton clusters [43, 66], vertical ionization prepares the corresponding ions in a configuration close to the most stable configuration of the neutral cluster. The energy spectrum of the $(Kr_n^+)^*$ parent ions electronic states for these configurations is presented in figure 12. It is strongly influenced by the symmetry of the neutral cluster configuration: the higher the symmetry of the neutral cluster structure, the larger the number of degeneracies in the ion electronic states. This can result in a small number of distinct energies, each one corresponding to a number of degenerate electronic states. Because of large energy separations these groups of electronic states are only weakly coupled to each other, resulting in a longer lifetime. This is the case for the lifetime maxima observed: $(Kr_4^+)^*$ has tetrahedral symmetry (T_d), and its 12 states group into five distinct energies; $(Kr_6^+)^*$ has octahedral symmetry (O_h), and its 18 states also group into five distinct energies; and $(Kr_{13}^+)^*$ has icosahedral symmetry (I_h) and its 39 states group into 11 distinct energies. On the other hand, $(Kr_8^+)^*$ which corresponds to the minimum of the lifetime curve only has C_s symmetry (reflection through the plane orthogonal

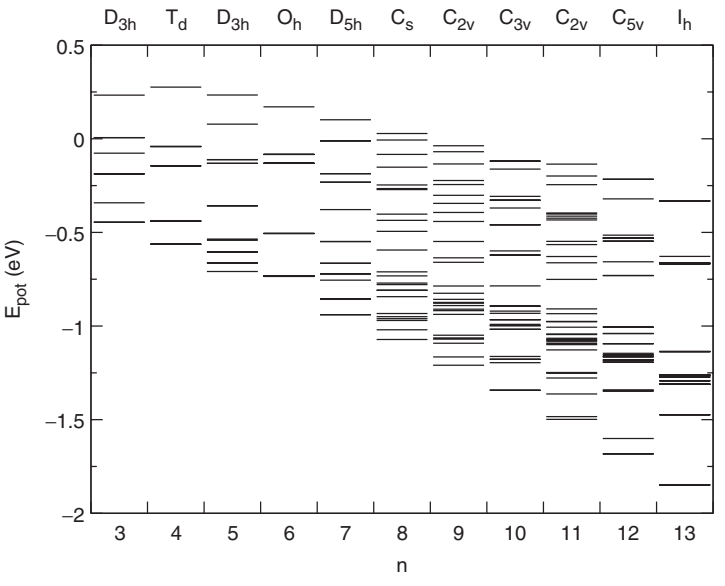

Figure 12. Potential energy spectrum of $(Kr_n^+)^*$ ($n = 3$–13) associated with the most stable configuration of Kr_n clusters (the SO interaction is neglected). The symmetry group for each configuration is specified at the top of the figure.

to the main axis of the cluster). The fragmentation efficiency of the parent ions therefore strongly depends on the configuration of initial neutral clusters.

When the SO interaction is included, the $(Kr_8^+)^*$ lifetime still corresponds to a minimum but no specific behaviour is visible for $(Kr_4^+)^*$ nor $(Kr_6^+)^*$. The inclusion of the relativistic correction removes some degeneracies: in the case of $(Kr_6^+)^*$ the number of distinct energies changes from five (from 18 states) to 12 over the 18 a priori possible values (doubly degenerated energy levels). The same is true for $(Kr_4^+)^*$: eight distinct energies over the 12 a priori possible values (12 doubly degenerated energy levels), compared to five distinct energies (from 12 states) when the SO interaction is neglected. Including the SO interaction therefore makes the fragmentation of the highly symmetric parent ions more efficient by lifting the degeneracy between their electronic states. With more distinct electronic states, which are on average closer to each other, non-adiabatic couplings are stronger and hence electronic relaxation is more efficient. A faster electronic relaxation brings more energy to the nuclear coordinates and fragmentation is faster.

This influence of the symmetry of the neutral precursor is not seen for neon and argon, even though all the neutral rare-gas clusters have the same equilibrium configuration. This is due to the effect of the neutral cluster ZPE, which determines the initial conditions for the ionic cluster dynamics. Initial conditions are determined by running a classical trajectory for the neutral cluster with a total energy equal to its ZPE, and assuming a vertical ionization at regular time intervals. In the krypton cluster case, the ZPE is so weak ($\sim 8\%$ of the potential well) that the dynamics of ionized krypton clusters starts very close from the most stable configuration of the neutral clusters. Neon clusters have a high ZPE ($\sim 40\%$ of the potential well) and a light mass: therefore

the parent ion dynamics starts from configurations far from the most stable neutral ones. For instance, the trimer $(Ne_3^+)^*$ starts from initial configurations ranging from an equilateral triangle to a linear structure, whereas all the initial krypton trimer configurations are very close to the equilateral triangle. As a consequence, no effect of the initial neutral cluster symmetry can be seen on the $(Ne_n^+)^*$ lifetimes. Argon clusters, with a ZPE around 15% of their potential well, are intermediate between neon and krypton clusters. Some symmetry effects are still noticeable: a first maximum for $n=4$, a minimum for $n=10$ and a second maximum for the icosahedral structure ($n=13$).

The inclusion of the SO interaction in the neon cluster dynamics leads to a systematic albeit modest acceleration of the parent ion fragmentation for all sizes. This is not the case for argon and krypton clusters, even though the SO splitting is about twice larger for argon ($\Delta E = 1431.5831\,\mathrm{cm}^{-1}$) than for neon ($\Delta E = 780.424\,\mathrm{cm}^{-1}$) and four times larger for krypton ($\Delta E = 5370.1\,\mathrm{cm}^{-1}$) than for argon. This may be due to two competitive effects. On the one hand the SO interaction, which is an additional coupling, tends to speed up electronic relaxation and fragmentation, on the other hand the gap between electronic states due to the SO splitting tends to slow down the relaxation. This would explain why only the highly symmetrical krypton clusters ($n=4$ and $n=6$) have their lifetimes shortened upon inclusion of the SO interaction.

Based on our results, we can predict that the lifetime of the larger krypton parent ions corresponding to highly symmetric configurations of the neutral cluster will be longer than that of similar size clusters. The same behaviour should be even enhanced for heavier rare-gas clusters like xenon, which have a still smaller ZPE.

5.1.2 Fragment stabilization time. We now turn to another characteristic time of the fragmentation dynamics of rare-gas clusters, the time needed to reach stable fragments, and therefore complete the dynamics. The time t_{form} needed to stabilize Rg_2^+ fragments coming from the electron-impact ionization of Rg_4, Rg_6, and Rg_8 are reported in table 3. t_{form} is obtained by fitting the Rg_2^+ appearance curve to an exponential function

$$g(t) = A\left(1 - \exp\left[\frac{-(t - t_0)}{t_{\mathrm{form}}}\right]\right) \tag{7}$$

where A is fixed to the asymptotic Rg_2^+ abundance and t_0 is the time delay for the appearance of the first fragment. Also reported in table 3 are the values for $t_{\mathrm{stab}}(X\%)$, the time needed to stabilize $(100 - X)\%$ of Rg_2^+ fragments (rounded off to the picosecond).

The most striking result is the change in time scales between neon, argon, and krypton clusters. The production of Rg_2^+ fragments is two to three times slower for argon than for neon and three to five times slower for krypton than for neon as shown by the t_{form} values. The stabilization time also depends on the initial cluster size: the larger the cluster, the slower the dynamics. This behaviour contrasts with that of the parent ion lifetimes, which decrease with increasing parent ion size for neon clusters and exhibit a minimum for argon ($n=10$) and krypton ($n=8$) clusters. Hence the fragment stabilization dynamics primarily slows down with cluster size,

Table 3. Stabilization time t_{stab} and time constant t_{form} in picoseconds for the most abundant fragment, i.e., Rg_2^+, coming from the ionization of Rg_4, Rg_6 and Rg_8 clusters. The upper and lower halves of the table correspond to calculations neglecting and including the SO interaction, respectively.

	Rg_n	t_{form}	t_{stab} (2%)	t_{stab} (1%)
W	Ne_4	0.90 ± 0.03	5	6
I	Ne_6	1.10 ± 0.02	6	8
T	Ne_8	1.40 ± 0.02	8	11
H				
O	Ar_4	2.02 ± 0.07	10	14
U	Ar_6	2.76 ± 0.05	18	25
T	Ar_8	4.23 ± 0.05	30	39
S	Kr_4	2.89 ± 0.11	16	23
O	Kr_6	4.36 ± 0.10	30	41
	Kr_8	7.00 ± 0.27	45	66
	Ne_4	0.76 ± 0.03	4	5
	Ne_6	1.00 ± 0.02	6	7
W	Ne_8	1.31 ± 0.04	7	8
I				
T	Ar_4	1.71 ± 0.05	9	11
H	Ar_6	2.70 ± 0.05	17	30
	Ar_8	4.16 ± 0.06	32	47
S				
O	Kr_4	2.32 ± 0.10	11	14
	Kr_6	4.65 ± 0.08	30	53
	Kr_8	6.76 ± 0.30	51	60

whereas this size dependence is inverted and modulated by the initial neutral cluster symmetry (particularly visible on krypton clusters) for parent ion fragmentation. This can be understood as follows. The increased number of coupled electronic states with parent ion size accelerates electronic state relaxation: the closer the electronic states, the larger the non-adiabatic couplings, hence the faster the electronic relaxation. This explains why the parent ion lifetimes tend to decrease with size. This first electronic relaxation step was shown to be complete in about 1 ps for neon clusters [42]. Thereafter all the dynamics occurs on the ground electronic state. Larger clusters have more degrees of freedom, which makes it more difficult to find the exit channel for fragmentation, hence the time required to reach stable fragments increases with cluster size.

Two effects have thus been highlighted: (i) an increased parent ion relaxation and fragmentation rate with cluster size due to the increased density of coupled electronic states, this effect being modulated by the symmetry of the neutral precursors when the ZPE is small; and (ii) a slower final fragmentation stage for larger clusters due to the larger number of degrees of freedom. The inclusion of the SO interaction does not affect these conclusions. Neon parent ions decay faster and lead to a faster production of fragments (about one picosecond less) when including the relativistic correction. For argon and krypton parent ions, fragmentation is faster only for the tetramer (tetrahedral configuration). This is another manifestation of the two competitive effects of the spin–orbit interaction: improvement of the relaxation efficiency because of the additional couplings between electronic states and slowing down of the relaxation due to the large SO splitting.

5.2 *Fragmentation mechanism*

We have seen in figure 10 of the preceding section that the fragmentation of ionized rare-gas clusters is sequential, subjected to configurational and size effects. We now turn to specify whether this fragmentation is rather evaporative or explosive. This problem has been treated in former publications [42, 43] on neon and krypton clusters. We generalize these results to the whole set of Rg_n^+ clusters that we have studied.

The most abundant neutral fragments are by far the monomers. For instance, in the case of $(Ne_9^+)^*$, $(Ar_9^+)^*$ and $(Kr_9^+)^*$, the abundance in neutral dimers and trimers is only about 0.6%, 2.3% and 3.3% of the total number of atoms ejected during the fragmentation, respectively. Figure 13 compares the mean number of fragmentation events per trajectory to the mean number of fragmentation events characterizing an atom by atom evaporation as a function of parent ion size. For all rare gases, there are fewer fragmentation events than for a pure atom by atom evaporation. Since most neutral fragments are monomers, this must be due to several atoms departing during the same fragmentation event. The fragmentation therefore appears explosive rather than evaporative.

Another argument confirms the rather explosive nature of the fragmentation of electron impact ionized rare-gas clusters. Figures 14(a) and 14(b) present the average kinetic energy per degree of freedom available to the $(Rg_n^+)^*$ parent ions and the average kinetic energy available to the Rg_2^+ fragments, respectively, as a function of cluster size. The Rg_2^+ available kinetic energy is much smaller than the total kinetic energy initially available for the parent ions. For instance, there is about 1.5 eV (0.25 eV per degree of freedom) of kinetic energy available for the parent ion $(Kr_4^+)^*$, and about 0.5 eV in the Kr_2^+ fragment, i.e. about 2/3 of the available kinetic energy (1 eV) has been dissipated during the dissociation. However, the energy of the dimer fragments is much larger than the parent ion energy per degree of freedom (see figure 14(a)) for all cluster sizes. In an evaporative process the ionic subsystem would cool down by

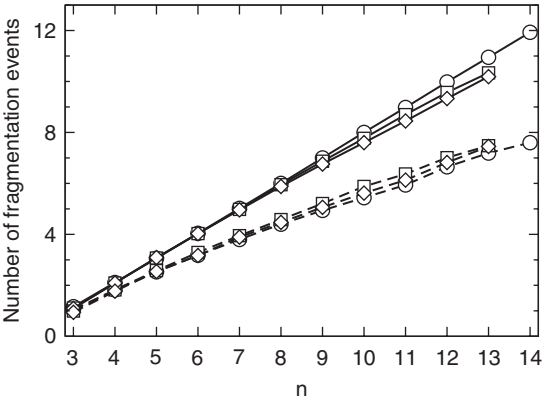

Figure 13. Comparison between the mean number of fragmentation events per trajectory (dashed curves) and the number of fragmentation events characterizing an atom by atom evaporation (solid curves) as a function of the parent ion size ($n = 3$–14) for neon (circles), argon (squares) and krypton (diamonds) clusters. Only trajectories that have lead to stable fragments are taken into account and the SO interaction is neglected.

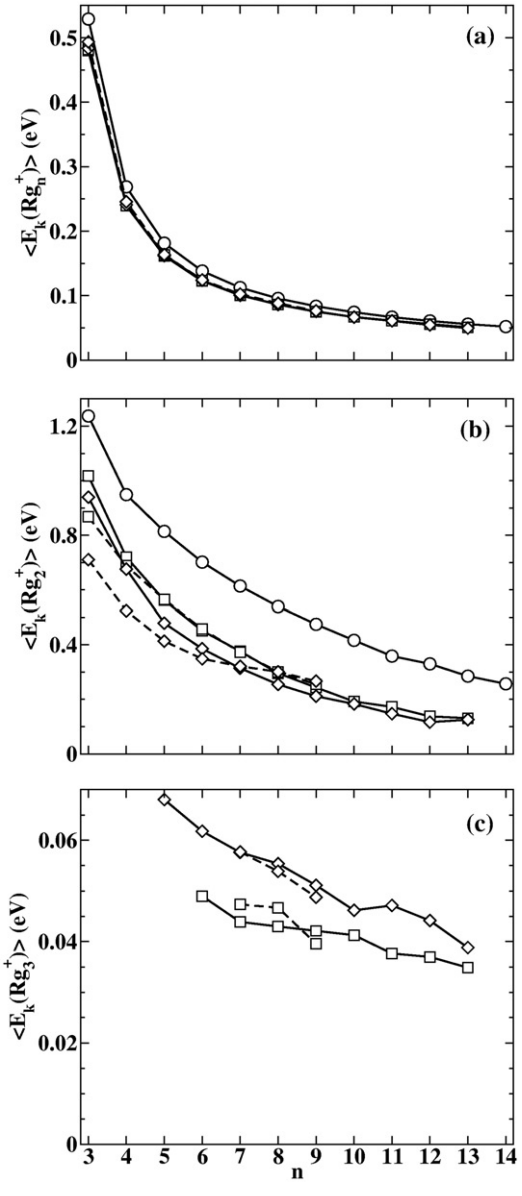

Figure 14. Kinetic energy per degree of freedom initially available for parent ion fragmentation (a), and for Rg_2^+ (b), and Rg_3^+ fragments (c). Rg = Ne (circles), Ar (squares), Kr (diamonds). The simulations neglected (solid curves) or included (dashed curves) the SO interaction.

atomic evaporation, i.e. the average kinetic energy per degree of freedom would decrease for each departing atom. This is clearly not the case, which shows that the internal energy does not have time to be redistributed over all the degrees of freedom.

We can also see in figure 14(a) that the available kinetic energy per degree of freedom in the parent ions is not significantly modified by the inclusion of the SO interaction.

This means that the average potential energies reached upon ionization are not affected by this correction. Note that neon clusters always have more kinetic energy than argon or krypton clusters. This is directly related to the vertical ionization process. Franck–Condon excitation from the neutral configurations leads to ionized neon clusters in the asymptotic regions of the electronic state curves because of the differences in equilibrium distances between neutral and ionic clusters. In the case of argon and krypton clusters the region reached upon ionization is less asymptotic since the C_4/R^4 asymptotic term of the Rg_2^+ ion-dipole interaction is larger than for neon.

We can also note that the inclusion of the SO interaction does not affect the results obtained for argon clusters, except for $n = 3$, whereas this interaction has a significant effect on krypton clusters. For $n \leq 6$, the Kr_2^+ fragment kinetic energy is weaker with the SO correction than without. For larger clusters this tendency is reversed. Since the SO interaction has little effect on the fragmentation rate of the $(Kr_n^+)^*$ parent ions and on Kr_2^+ stabilization times (see section 5.1), finding a reason for this behaviour is not obvious. When the SO interaction is included in the dynamics, the number of electronic states changes from $3n$ to $6n$. We can advance that doubling the number of electronic states should provide a better energy relaxation. This effect should be more important for the smallest clusters since they have a higher parent ion internal energy per degree of freedom. However, it should also be true for argon clusters and this is not the case. One reason could be that since fragmentation is slower for krypton than for argon clusters (see figure 10 and table 3), this can provide enough time to the system to improve its thermalization between two fragmentations.

Figure 14(c) presents the kinetic energy per degree of freedom available to Rg_3^+ fragments as a function of the parent ion size. No result concerning neon clusters is reported because the Ne_3^+ fragments abundance is too small. The decrease in the kinetic energy of Rg_3^+ fragments with increasing parent ion size is due to the fact that larger parent ions lose more atoms and consequently more kinetic energy to lead to triatomic fragments. The kinetic energy of Ar_3^+ fragments is clearly smaller than that of Kr_3^+ fragments. This can originate from the energy difference between the minima of the Rg_3^+ and Rg_2^+ ground state potential-energy curves (Rg = Ar and Kr): it is about 0.18 eV for argon clusters [44] and 0.24 eV for krypton clusters [43]. This sets a limit of 0.06 eV and 0.08 eV for the kinetic energy per degree of freedom of Ar_3^+ and Kr_3^+ respectively (a Rg_3^+ fragment is considered stable when its internal energy is below the classical minimum energy of Rg_2^+). Kr_3^+ fragments can thus take away a kinetic energy larger than that of Ar_3^+ fragments. Finally, the SO interaction has no relevant effect on Rg_3^+ kinetic energies. This observation shows that this interaction mainly affects the Rg^+ and Rg_2^+ fragment abundances but has no significant effect on larger fragments (see section 5.4).

5.3 *Existence of long-lived trajectories*

The fragment proportions presented in figure 9 do not sum up to 100%. This comes from the existence of long-lived trajectories that reach the time limit, i.e. 100 ps, with intermediate species that are still able to fragment. The proportion of these trajectories is shown in figure 15 as a function of parent ion size ($n = 2$–14) for neon, argon

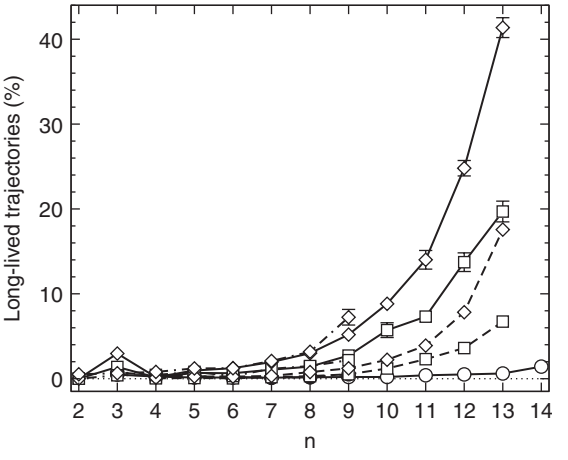

Figure 15. Proportion of long-lived trajectories for neon (circles), argon (squares) and krypton (diamonds) clusters as a function of the parent ion size ($n = 2$–14): after a 100 ps mixed quantum–classical propagation (solid curves without and dashed-dotted curves with SO interaction), and after an additional 10 ns adiabatic propagation on the ground electronic state of the system (dashed curves). Statistical uncertainties are only specified when they exceed the size of plotting symbols.

and krypton clusters. The first remarkable feature is the sharp increase for $n > 7$ and $n > 6$ for argon and krypton clusters respectively. For smaller clusters, these trajectories contribute to at most 1% of the whole number of trajectories (except for the particular case of $n = 3$ without SO coupling which was discussed above). The proportion of these trajectories reaches $19.7 \pm 1.2\%$ for $(Ar_{13}^+)^*$ and $41.4 \pm 1.2\%$ for $(Kr_{13}^+)^*$. For $n \geq 7$, these trajectories correspond to $(Rg_p^+)^*$ ($p \leq n$) intermediate species that evolve on their ground electronic state with an internal energy above the dissociation limit. We have checked for krypton clusters that hardly 5–10% of these long-lived trajectories evolve in the attraction basin of an excited isomer (the attraction basin of a given isomer is defined as the phase space region for which a local energy minimization leads to the minimum energy of the isomer). The rest corresponds to trajectories that evolve in the attraction basin of the most stable isomer of the intermediate species. Proportions of $(Rg_p^+)^*$ (Rg = Ar and Kr, $p \geq 3$) excited intermediate species are collected in table 4. These species are obtained after a 100 ps mixed quantum–classical propagation of Rg_n ($n \geq 7$) clusters ionized by electron impact. Their size increases with the parent ion size and the mass of the rare gas considered. For instance, from the 19.70% of long-lived trajectories coming from the ionization of Ar_{13}, 30% correspond to $(Ar_3^+)^*$ and 7% correspond to species with more than six atoms. For Kr_{13} hardly 5% of long-lived trajectories correspond to $(Kr_3^+)^*$ and 27% correspond to species with more than six atoms. Note that neon clusters are not examined here because their long-lived trajectories proportion never exceeds 1.5% and their study would thus not be statistically significant.

We can surmise that the existence of long-lived trajectories is related to the production of larger fragments. Kr_3^+ fragments start appearing for $n \geq 5$ which coincides with the increase in the amount of long-lived trajectories. This is also true for neon and argon clusters: for Ne_{14}, the abundance in Ne_3^+ fragment equals 6.17% and the

Table 4. Percentage of long-lived trajectories, i.e., trajectories for which unstable intermediate species $(Rg_p^+)^*$ still evolve after a 100 ps propagation, and relative abundances of the intermediate species at $t = 100$ ps. These proportions are normalized to 100% and the SO interaction is not taken into account.

Rg_n	Long-lived trajectories	$(Rg_3^+)^*$	$(Rg_4^+)^*$	$(Rg_5^+)^*$	$(Rg_6^+)^*$	$(Rg_p^+)^*$ $(p \geq 7)$
Ar_7	1.06 ± 0.19	98	2	0	0	0
Ar_8	1.42 ± 0.14	93	7	0	0	0
Ar_9	2.72 ± 0.13	67	27	5	1	0
Ar_{10}	5.72 ± 0.87	54	35	9	0	2
Ar_{11}	7.31 ± 0.29	33	40	16	8	3
Ar_{12}	13.73 ± 1.10	41	23	13	7	2
Ar_{13}	19.70 ± 1.22	30	26	14	10	7
Kr_7	1.96 ± 0.16	99	1	0	0	0
Kr_8	3.00 ± 0.18	87	12	1	0	0
Kr_9	5.19 ± 0.31	67	26	5	2	0
Kr_{10}	8.82 ± 0.78	35	49	14	2	0
Kr_{11}	14.01 ± 1.10	19	37	29	10	5
Kr_{12}	24.80 ± 0.91	10	27	23	20	20
Kr_{13}	41.37 ± 1.17	5	25	28	15	27

Table 5. Abundances in Ar_p^+ fragments (%) obtained after additional 1 and 10 ns adiabatic propagations of the long-lived trajectories on the ground electronic state of the system. The last column gives the proportion of trajectories that have not reached stable fragments at the end of the additional propagation. The SO interaction is not taken into account.

Additional propagation time (ns)	Ar_n	Ar_2^+	Ar_3^+	Ar_4^+	Ar_p^+ $(p \geq 5)$	Long-lived trajectories
1	Ar_7	66.04	1.89	0	0	32.08
	Ar_8	46.48	7.04	0	0	46.48
	Ar_9	43.38	16.91	4.41	0	35.29
	Ar_{10}	29.82	17.54	7.02	0	45.61
	Ar_{11}	16.44	23.29	5.48	4.11	50.68
	Ar_{12}	8.76	25.55	10.22	13.14	42.34
	Ar_{13}	7.65	15.82	12.76	12.75	51.02
10	Ar_7	80.77	1.92	0	0	17.31
	Ar_8	69.23	7.69	0	0	23.08
	Ar_9	50.76	24.24	5.30	0	19.70
	Ar_{10}	45.61	24.56	8.77	0	21.05
	Ar_{11}	20.55	31.51	9.59	6.85	31.51
	Ar_{12}	10.22	34.31	12.41	16.79	26.28
	Ar_{13}	8.67	21.94	18.88	16.33	34.18

proportion of long-lived trajectories reaches 1.42%, which is quite close to the case of Ar_8 (5.75% of Ar_3^+ fragments and 1.42% of long-lived trajectories) and Kr_7 (6.44% of Kr_3^+ fragments and 1.96% of long-lived trajectories).

In order to get a better understanding of the role played by long-lived trajectories, we have propagated them adiabatically on the ground electronic state during an extra 1 and 10 nanoseconds. Ar_p^+ and Kr_p^+ fragment proportions obtained after these additional propagations are reported in tables 5 and 6 respectively. After a

Table 6. Abundances in Kr_p^+ fragments (%) obtained after additional 1 and 10 ns adiabatic propagations of the long-lived trajectories on the ground electronic state of the system. The last column gives the proportion of trajectories that have not reached stable fragments at the end of the additional propagation. The SO interaction is not taken into account.

Additional propagation time (ns)	Kr_n	Kr_2^+	Kr_3^+	Kr_4^+	Kr_p^+ ($p \geq 5$)	Long-lived trajectories
1	Kr_7	63.27	0	0	0	36.73
	Kr_8	45.64	5.37	1.34	0	47.65
	Kr_9	37.07	17.76	3.86	0.39	40.93
	Kr_{10}	21.59	27.27	7.95	2.27	40.91
	Kr_{11}	10.00	25.00	12.86	7.14	45.00
	Kr_{12}	4.86	12.96	10.93	14.57	56.68
	Kr_{13}	2.18	16.99	13.59	9.71	57.52
10	Kr_7	81.52	1.09	0	0	17.39
	Kr_8	62.59	9.52	1.36	0	26.53
	Kr_9	46.80	23.60	4.80	0.40	24.40
	Kr_{10}	24.14	36.78	11.49	2.30	25.29
	Kr_{11}	14.39	28.78	18.71	10.07	28.06
	Kr_{12}	7.29	19.84	17.00	24.29	31.58
	Kr_{13}	2.43	19.67	18.93	16.50	42.48

10 ns propagation, the number of long-lived trajectories is on average a factor of two smaller than after a 1 ns propagation.

Figure 16 presents Rg^+, Rg_2^+, Rg_3^+ and Rg_4^+ fragment abundances obtained after a 100 ps mixed quantum–classical propagation, followed by a 10 ns adiabatic propagation when the dynamics was not completed at $t = 100$ ps. Abundances in ionic monomers are not modified by the contribution of long-lived trajectories: these fragments come from rather fast dissociations that occur when the dynamics involves a highly energetic excited state [43, 44, 63]. Abundances in ionic dimers Rg_2^+ (Rg = Ar and Kr) change very slightly when including long-lived trajectories, but the qualitative behaviour of Rg_2^+ proportion curves is not affected (see figure 16). The first relevant differences appear for fragments with more than three atoms. In particular, figure 16(d) reveals that the abundance in ionic tetramer Kr_4^+ is more than doubled for larger parent ion sizes when the contribution of long-lived trajectories is included. These modifications are limited to larger clusters and do not consequently affect the general trends deduced from calculations performed during the first 100 ps, at least for fragments with less than four atoms. Finally, these trajectories are certainly the manifestation of an evaporative mechanism starting to take place in the dynamics of larger parent ions on long time scales.

5.4 *Effect of the spin–orbit interaction*

The SO interaction is described using the semiempirical treatment by Cohen and Schneider [60], which was illustrated on Xe_n^+ clusters by Amarouche *et al.* [59]. The SO Hamiltonian is expressed as

$$\hat{H}_{SO} = A\vec{L} \cdot \vec{S} \tag{8}$$

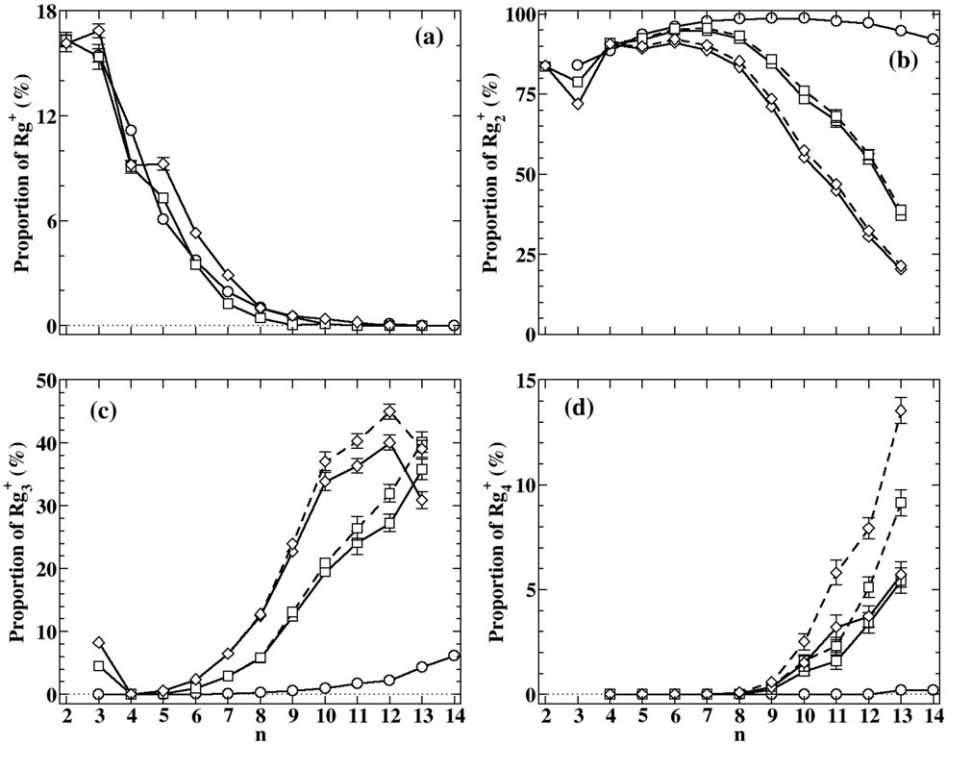

Figure 16. Theoretical abundance (%) in (a) Rg^+ , (b) Rg_2^+, (c) Rg_3^+ and (d) Rg_4^+ fragments as a function of the initial cluster size ($n = 2$–14). Solid curves correspond to results obtained after a 100 ps mixed quantum–classical propagation for neon (circles), argon (squares) and krypton (diamonds) clusters. Dashed curves correspond to proportions that take into account long-lived trajectories which have fragmented after an additional 10 ns adiabatic propagation on the ground electronic state of the system. Statistical uncertainties are only specified when they exceed the size of plotting symbols. The spin–orbit coupling is neglected.

where $A = -\frac{2}{3}\Delta E$, ΔE being the SO splitting between the $^2P_{3/2}$ and $^2P_{1/2}$ Rg^+ states, $\vec{L}$ is the orbital angular momentum and $\vec{S}$ the electronic spin. The spin–orbit splitting ΔE is equal to 780.424 cm^{-1}, 1431.5831 cm^{-1} and 5370.1 cm^{-1} for neon, argon, and krypton ionic monomers, respectively [58].

As can be seen in figure 9, the SO interaction does not affect the general trends of the fragment proportions except for $n = 3$. In this case, the SO interaction couples the A′ and A″ states which are otherwise uncoupled (they could be coupled by overall rotation but the calculations presented here are for zero total angular momentum). For argon and krypton trimers, one of the A″ states has a well in the Franck–Condon region for vertical ionization, which leads to metastable $Rg_3^+(A'')$ fragments in the absence of SO coupling. These fragments no longer appear when A′ and A″ states are coupled. Although the qualitative behaviour of the fragment proportion curves in figure 9 is generally conserved, figure 9(a) and 9(b) show that the SO interaction favours the formation of Rg^+ fragments at the expense of Rg_2^+ fragments and that the difference decreases with parent ion size.

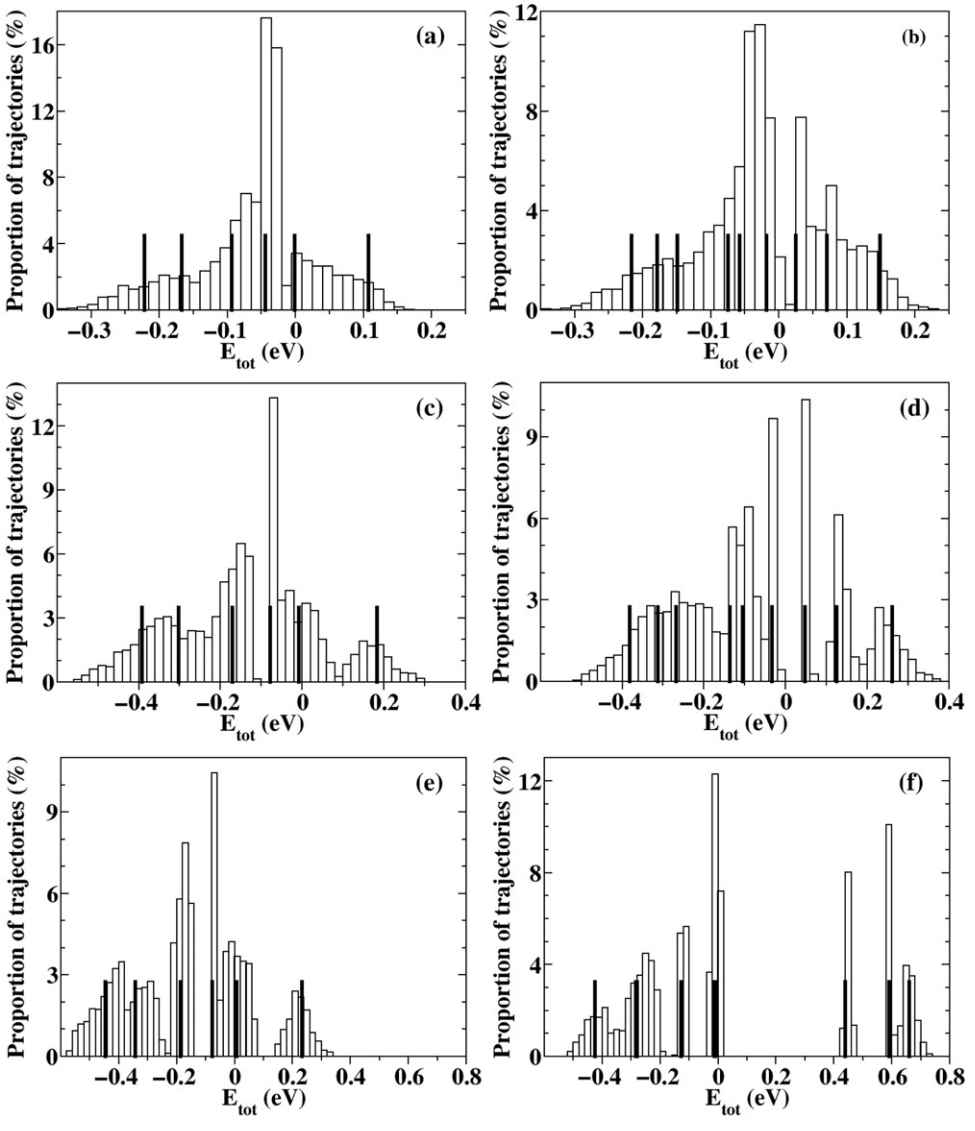

Figure 17. Total energy distributions of $(Ne_3^+)^*$ (plots a and b), $(Ar_3^+)^*$ (plots c and d), $(Kr_3^+)^*$ (plots e and f) when neglecting (left column) and including (right column) the SO interaction. The thick curves represent the total energies for the most stable Rg_3 configuration in the different electronic states of Rg_3^+. Plots (a) and (b) are reproduced from [42], figure 6, and plots (e) and (f) from [43], figure 8, with permission.

As expected, the effect of the SO interaction increases with its magnitude. One reason for this is based on the total energy distributions. They are presented in figure 17 for $(Ne_3^+)^*$, $(Ar_3^+)^*$ and $(Kr_3^+)^*$, neglecting or including the SO interaction. Since the initial conditions originate from vertical ionization of the neutral cluster, they correspond to configurations close to the asymptotic region where the $(Rg_n^+)^*$ states correlate to the $Rg^+(^2P) + (n-1)\,Rg$ dissociation limit. Inclusion of the SO coupling splits the

$Rg^+(^2P)$ level into $^2P_{1/2}$ and $^2P_{3/2}$, which creates two subsets of electronic states correlating to the corresponding dissociation limits. The subset correlating with the excited SO state induces initial conditions with a higher total energy on average. This is particularly clear for Kr^+, which has a SO splitting of $5370.1\,cm^{-1}$ (see figures 17(e) and (f)). Since the spin–orbit splitting is smaller than the Rg_2^+ well depth, even for krypton, transitions between SO states are efficient. Inclusion of the SO coupling increases the number of trajectories with positive total energy, which are the only ones that can lead to monomer fragments. Hence, the increased monomer fragment proportion originates from energetic reasons. Potential energies corresponding to the most stable configurations of the initial neutral cluster are also specified (thick lines) in figure 17.

The SO interaction does not significantly affect Rg_p^+ $(p \geq 3)$ proportions (see figures 9(c) and (d)). Rg_p^+ $(p \geq 3)$ fragments are mostly generated in trajectories for which the system has relaxed to its ground electronic state: once the ground state is reached, the SO interaction does not seem to influence the ability of the system to find its way to stable fragments.

Finally, it is worth noting that the inclusion of the SO interaction in the dynamics of krypton clusters quantitatively modifies the monomer and dimer proportions for all cluster sizes investigated. This behaviour is not found for neon and argon clusters. It is thus essential to take into account the SO interaction in order to simulate the dynamics of krypton clusters and *a fortiori* the dynamics of heavier clusters like xenon clusters.

6. Discussion of the comparison between theory and experiment

The comparison of the detailed calculations with the experimental results for Ar_n and Kr_n clusters reveals that the general trends, severe fragmentation, the predominance of the dimer and monomer ion channels, and the threshold for the appearance of the trimer ion channel at $n = 5$ of the neutral precursor, are correctly predicted. However, if we look at the details, especially at the relative amount of the dimer to the monomer ion channel, some discrepancies appear. In the case of Ar_n, experiment and theory are in good agreement. The experimental results for the smaller clusters $n = 2$ and $n = 3$ are well reproduced in the simulation, and the dimer ion was primarily the largest channel both in the calculation and in the experiment. The fluctuations of the experiment, which do not show up in the calculations, are very probably due to experimental uncertainties. Interestingly, the remaining discrepancies disappear when the corrections of the secondary ionization of neutral monomer fragments is applied. Although this is not a stringent proof, the results look very convincing.

For Kr_n clusters the situation is not as satisfactory as for the Ar_n case. Here the calculations exhibit the predominance of the Kr_2^+ channel increasing from 50% to 80%, while the experiments present the monomer Kr^+ ion as main channel with probabilities larger than 90%. The correction due to the secondary ionization of neutral monomer fragments, which worked so well for Ar_n, does not really help, since the problem occurs already for the dimer. The calculations in this case correctly predict the evolution of the monomer fragment proportion as a function of the rare gas

nature, with 35% for argon and 50% for krypton, but not the surprising dominance of 95% for Kr^+.

Possible sources for this discrepancy have already been discussed [44, 46]. We summarize them here and present new hypotheses. Let us briefly discuss first possible errors of the experiment with respect to the calculations. Experimental errors caused by finite resolution and data evaluation effects were estimated in [46] to be not larger than 5%. Similar considerations hold for the influence of collisional dissociation which would increase the amount of monomers. Estimations of the transferred energy [46] and the addition of energy in the simulation [43] lead to the conclusion that this effect is negligible. The effect of secondary ionization of neutral monomer fragments has already been discussed. It decreases the amount of monomers, especially for the larger clusters, but has no effect on the observed discrepancy for the dimer parent ions.

A limitation of the calculation is apparently the time scale of the trajectories. The time limit has been set to 100 ps in the mixed quantum–classical simulation, and long-lived trajectories, i.e. trajectories which had not reached stable fragments after 100 ps, were propagated classically for an additional 10 ns. In the experiment, however, time scales in the order of μs are available for the ions on their way from the ion source to the entrance of the quadrupole. This might lead to further evaporative processes resulting in Kr^+. However, for the smaller clusters ($n < 6$ for krypton, $n < 7$ for argon, all the studied sizes for neon) almost all the trajectories have reached stable fragments within the 100 ps time limit, which precludes any further evaporation. For the larger clusters, the calculated 'long-lived trajectories' tend to lead to larger fragments than the ones reaching stable fragments within the time limit of 100 ps. Therefore the long time scale of the experiment cannot affect the monomer fraction, and in particular not the one coming from the dimer ionization.

One possible source of errors in the simulation is the preference for downward hops in the MDQT method: a number of upward transitions are forbidden by energy conservation, and this is the main source of error compared with quantum simulations [67–69]. This could result in an overestimation of the electronic relaxation rate, which could lead to more violent kinetic energy relaxation in the initial steps of the fragmentation. This would leave the ionic core with too small internal energy to further fragment. However, this method gives good results for argon clusters, so it is difficult to understand why this possible source of error would become important for krypton. In addition, it could not explain the large amount of missing monomer fragments for the smallest parent ions since the number of fragmentation steps is very small for these sizes.

A possibility for increasing the calculated proportion of monomer ion fragments would be the preferential population of electronically excited states of the parent ions, in particular spin–orbit excited states. The smallest fragments mainly originate from trajectories initiated in the highest electronic states [43, 44, 63], and the spin–orbit excited states of the dimers all give monomer fragments by energy conservation. In the simulation it is assumed that all electronic states of the parent ion Kr_n^+ are equiprobably populated. However, larger clusters produce almost no monomer ions even for trajectories starting on the highest electronic states: for instance, the highest

electronic state of $(Ar_9^+)^*$ leads to less than 1% of Ar^+. It is also not conceivable why special states should be selected in the ionization process.

Another possibility to get a larger proportion of monomer fragments would be the production of higher excited states in the ionization process. All the states that correlate with $Rg^+(^2P_{3/2}) + (n-1)$ Rg and $Rg^+(^2P_{1/2}) + (n-1)$ Rg are included in the simulation. The next higher states in energy are the electronic states that correlate with $Rg^+(^2S) + (n-1)$Rg (which correspond to a hole in the next higher s orbital). They would certainly lead to more extensive fragmentation since they lie about 10 eV higher in energy. However, the electron-impact ionization cross-section of Rg to $Rg^+(^2S)$ is about 15 to 30 times lower than that to $Rg^+(^2P)$ for incident electron energies between 50 and 150 eV [70]. Assuming the same ratio for the ionization cross-sections in the cluster, this could only add about 5% of monomer fragments at most, which is far less than the difference between simulated and experimental results.

None of these possibilities appears to be effective enough to be responsible for the large discrepancy which occurs already for the fragmentation of the neutral krypton dimer Kr_2. Thus we are left for the moment with the problem why krypton dimers exhibit a larger fragmentation probability to monomer ions than argon dimers.

We suggest here several new hypotheses for mechanisms which could cause such a difference. There is a possibility to increase the monomer fraction if the potential energy curves for the dimer were different in the long-range part. If the majority of the ionic dimer potential curves were repulsive in that region, or only very slightly attractive, this would lead to an increased fragmentation, especially for the dimer. Another possibility is that the excess energy in the ionization process is not completely taken away by the electrons and a certain amount is left in the krypton clusters. This would require the modelling of the ionization process itself. However in this case we would have to understand why this is not true for argon clusters. A further option is the internal temperature of the clusters as they are formed during the isentropic expansion: for krypton clusters the condensation energy is a bit higher than for argon clusters. This effect might lead to a higher temperature of the krypton clusters and could lead to more dissociation.

7. Conclusion

We have reviewed the fragmentation of rare-gas clusters Rg_n ($2 \leq n \leq 14$ and Rg = Ne, Ar and Kr) upon electron-impact ionization. The accent was put on the confrontation of experimental and theoretical results. Therefore only experiments which size-selected the neutral clusters prior to ionization were considered, as well as only the most realistic simulations which included all the relevant electronic states of the ionic clusters and their couplings.

The comparison of the experimental and theoretical results for the argon and krypton clusters has revealed a very good agreement concerning the extensive character of the fragmentation, and the tendency to form larger fragments as the size of the neutral precursor increases. For argon clusters the agreement is quantitative, especially if the possibility for secondary neutral monomer ionization is taken into account. For krypton clusters there are some discrepancies concerning the monomer to dimer

fragment ion proportion. Several possible reasons for this discrepancies have been proposed and discussed.

After this validation of the simulation by comparison with the experimental results, a more detailed analysis of the theoretical results has been presented, including results for neon clusters for which no experimental results are yet available. This analysis has provided some crucial information concerning the kinetics of the fragmentation process and its mechanism. It was shown that fragmentation is very fast, on the timescale of picoseconds, and that it is closer to an explosive rather than evaporative mechanism. However, for the larger sizes of the argon and krypton clusters, some longer-lived trajectories start appearing. Their existence, together with their propensity to favour larger fragments, could indicate that an evaporative mechanism is starting to take place in large clusters.

We have also shown new results that help rationalizing the evolution of the characteristic lifetimes of the dynamics with parent ion size. The beginning of the dynamics is dominated by electronic relaxation rate, which is directly related to the density of coupled electronic states. Hence the parent ion lifetimes decrease on average with size (each new atom brings three additional electronic states). This propensity is modulated by the symmetry of the initial configuration, which results in groups of degenerate levels with weak inter-group coupling because of energy separation. The effect is strongest for krypton clusters for which the initial configuration of the parent ions is very close to that of the neutral precursors at equilibrium because of their small ZPE. Once electronic relaxation has taken place (about one picosecond), the second part of the fragmentation dynamics takes place in the ground electronic state of the intermediate species. In this second part, a larger number of degrees of freedom results in a longer time to find the exit channel to dissociation and hence to reach stable fragments.

We have characterized the fragmentation as explosive, rather than evaporative, based on two arguments. One was the existence of a number of dissociative events corresponding to the departure of more than one neutral atom. The other one was based on the analysis of the available kinetic energy per degree of freedom, which showed that even though a large energy was dissipated during the fragmentation dynamics, the available kinetic energy per degree of freedom ('internal temperature') was higher in the final products than in the parent ion.

It would be interesting to study larger clusters, both experimentally and theoretically, to determine when the threshold for evaporative fragmentation is taking place. The neutral $n = 13$ rare-gas cluster is a closed structure (icosahedron), but the resulting core trimer ion is not completely surrounded by neighbours. It may take another shell of rare-gas atoms in the neutral cluster to start seeing some important effects of hindered dissociation, and hence energy relaxation within the cluster which can lead to an evaporative mechanism.

It would also be interesting to obtain experimental results both for the lighter (neon) and heavier (xenon) rare gases. Neon clusters are predicted to be the most extensively fragmenting clusters. On the other hand, getting results on the xenon clusters could help understanding why the monomer fragments are so predominant in the krypton clusters. Preliminary results show that this is also the case for xenon clusters [71].

Acknowledgements

The authors would like to thank M. Fárník for fruitful discussions, for his strong interest in this work, and for the copy of figure 3 data prior to publication. They would also like to thank K.C. Janda for very helpful comments on the manuscript. The Toulouse (CALMIP) and the French (IDRIS-CINES) national computer centres are gratefully acknowledged for grants of computer time.

References

[1] H. Haberland, editor, *Clusters of Atoms and Molecules* (Springer, Berlin, 1994).
[2] M. Kappes and S. Leutwyler, in *Atomic and Molecular Beam Methods*, edited by G. Scoles, page 380 (Oxford, New York, 1988).
[3] A. J. Stace and A. K. Shukla, J. Mass Spectr. Ion Phys. **36**, 119 (1980).
[4] K. Stephan and T. D. Märk, Chem. Phys. Lett. **90**, 51 (1982).
[5] D. R. Worsnop, S. J. Buelow, and D. R. Herschbach, J. Phys. Chem. **88**, 4506 (1984).
[6] H. Haberland, Surf. Sci. **156**, 305 (1985).
[7] T. E. Gough and R. E. Miller, Chem. Phys. Lett. **87**, 280 (1982).
[8] J. Geraedts, S. Stolte, and J. Reuss, Z. Phys. A **304**, 167 (1982).
[9] D. D. Nelson Jr, G. T. Fraser, and W. Klemperer, J. Chem. Phys. **83**, 6201 (1985).
[10] J. B. Hopkins, D. E. Powers, and R. E. Smalley, J. Chem. Phys. **85**, 3739 (1981).
[11] S. Leutwyler, U. Even, and J. Jortner, Chem. Phys. Lett. **86**, 439 (1982).
[12] K. Rademann, B. Brutschy, and H. Baumgärtl, Chem. Phys. **83**, 129 (1980).
[13] U. Buck and H. Meyer, Phys. Rev. Lett. **52**, 109 (1984).
[14] U. Buck and H. Meyer, J. Chem. Phys. **84**, 4854 (1986).
[15] P. J. Kuntz and J. Valldorf, Z. Phys. D **8**, 195 (1988).
[16] T. Ikegami, T. Kondow, and S. Iwata, J. Chem. Phys. **98**, 3038 (1993).
[17] T. P. Martin, Phys. Rep. **95**, 167 (1983).
[18] T. D. Märk and O. Echt, Internal reactions and metastable dissociations after ionization of van der waals clusters, in *Clusters of Atoms and Molecules*, edited by H. Haberland, pages 154–182 (Springer, Berlin, 1994).
[19] U. Buck, C. Lauenstein, H. Meyer, and R. Sroka, J. Phys. C **92**, 1916 (1988).
[20] U. Buck, C. Lauenstein, R. Sroka, and M. Tolle, Z. Phys. D **10**, 303 (1988).
[21] U. Buck, G. Hoffmann, J. Kesper, D. Otten, and M. Winter, Chem. Phys. **126**, 159 (1988).
[22] L. Beneventi, P. Casavecchia, L. Y. Rusin, and G. G. Volpi, in *The Chemical Physics of Atomic and Molecular Clusters*, edited by G. Scoles, page 579 (North Holland, Amsterdam, 1990).
[23] U. Buck, M. Hobein, R. Krohne, and H. Linnartz, Z. Phys. D **20**, 181 (1991).
[24] J. Kreil, M.-W. Ruf, H. Hotop, I. Ettischer, and U. Buck, Chem. Phys. **239**, 459 (1998).
[25] Y. Ono, E. A. Osuch, and C. Y. Ng, J. Chem. Phys. **74**, 1645 (1981).
[26] U. Buck, H. Meyer, J. D. Nelson, G. Fraser, and W. Klemperer, J. Chem. Phys. **88**, 3028 (1988).
[27] U. Buck and C. Lauenstein, J. Chem. Phys. **92**, 4250 (1990).
[28] U. Buck and M. Winter, Z. Phys. D **31**, 291 (1994).
[29] R. Baumfalk, U. Buck, C. Frischkorn, S. R. Gandhi, and C. Lauenstein, Ber. Bunsenges. Phys. Chem. **101**, 606 (1997).
[30] M. Fárník, M. Weimann, C. Steinbach, U. Buck, N. Borho, T. B. Adler, and M. A. Suhm, Phys. Chem. Chem. Phys. **8**, 1148 (2006).
[31] S. Tomoda and K. Kimura, Chem. Phys. **110**, 431 (1986).
[32] U. Buck, J. Phys. Chem. **92**, 1023 (1988).
[33] U. Buck, in *The Chemical Physics of Atomic and Molecular Clusters*, edited by G. Scoles, page 543 (North Holland, Amsterdam, 1990).
[34] L. Bewig, U. Buck, C. Mehlmann, and M. Winter, J. Chem. Phys. **100**, 2765 (1994).
[35] I. V. Hertel, C. P. Schulz, A. Goerke, H. Palm, and G. Leipelt, J. Chem. Phys. **107**, 2528 (1997).
[36] J. M. Soler, J. J. Sáenz, N. Garcia, and O. Echt, Chem. Phys. Lett. **109**, 71 (1984).
[37] J. J. Sáenz, J. M. Soler, and N. García, Surf. Sci. **156**, 121 (1985).
[38] P. Stampfli, Z. Phys. D **40**, 345 (1997).
[39] P. J. Kuntz and J. J. Hogreve, J. Chem. Phys. **95**, 156 (1991).

[40] A. Bastida, N. Halberstadt, J. A. Beswick, F. X. Gadéa, U. Buck, R. Galonska, and C. Lauenstein, Chem. Phys. Lett. **249**, 1 (1996).
[41] D. Bonhommeau, A. Viel, and N. Halberstadt, J. Chem. Phys. **120**, 11359 (2004).
[42] D. Bonhommeau, A. Viel, and N. Halberstadt, J. Chem. Phys. **123**, 054316 (2005).
[43] D. Bonhommeau, T. Bouissou, N. Halberstadt, and A. Viel, J. Chem. Phys. **124**, 164308 (2006).
[44] D. Bonhommeau, N. Halberstadt, and A. Viel, J. Chem. Phys. **124**, 184314 (2006).
[45] P. Lohbrandt, R. Galonska, H. Kim, M. Schmidt, C. Lauenstein, and U. Buck, Electron Impact Fragmentation of Size Selected Ar_n ($n=4$ to 9) Clusters, in *Atomic and Molecular Beams: The State of the Art 2000*, edited by R. Campargue, pages 623–636 (Springer, Berlin, 2001).
[46] C. Steinbach, M. Fárník, U. Buck, C. A. Brindle, and K. C. Janda, J. Phys. Chem. A **110**, 9108 (2006).
[47] F. O. Ellison, J. Am. Chem. Soc. **85**, 3540 (1963).
[48] F. O. Ellison, N. T. Huff, and J. C. Patel, J. Am. Chem. Soc. **85**, 3544 (1963).
[49] W. R. Wadt, Appl. Phys. Lett. **38**, 1030 (1981).
[50] J. C. Tully, J. Chem. Phys. **93**, 1061 (1990).
[51] J. C. Tully, Int. J. Quant. Chem. Quant. Chem. Symp. **25**, 299 (1991).
[52] S. Hammes-Schiffer and J. C. Tully, J. Chem. Phys. **101**, 4657 (1994).
[53] D. Hrivňák, R. Kalus, and F. X. Gadéa, Europhys. Lett. **71**, 42 (2005).
[54] I. Janeček, D. Hrivňák, R. Kalus, and F. X. Gadéa, J. Chem. Phys. **125**, 104315 (2006).
[55] R. Kalus, F. X. Gadéa, *et al*., private communication.
[56] R. A. Aziz and M. J. Slaman, Mol. Phys. **58**, 679 (1986).
[57] R. A. Aziz and M. J. Slaman, Chem. Phys. **130**, 187 (1989).
[58] T. H. Ha, P. Rupper, A. Wüest, and F. Merkt, Mol. Phys. **101**, 827 (2003).
[59] M. Amarouche, G. Durand, and J. P. Malrieu, J. Chem. Phys. **88**, 1010 (1988).
[60] J. S. Cohen and B. Schneider, J. Chem. Phys. **61**, 3230 (1974).
[61] M. F. Herman and E. Kluk, Chem. Phys. **91**, 27 (1984).
[62] M. F. Herman, J. Chem. Phys. **81**, 754 (1984).
[63] D. Bonhommeau, N. Halberstadt, and A. Viel, J. Chem. Phys. **124**, 024328 (2006); also selected for publication in the Virtual Journal of Nanoscale Science and Technology, **13** (3), 23 January 2006.
[64] U. Buck, F. Huisken, J. Schleusener, and J. Schäfer, J. Chem. Phys. **72**, 1512 (1980).
[65] V. Poterya and M. Fárník, (2006), unpublished results.
[66] D. M. Leitner, J. D. Doll, and R. M. Whitnell, J. Chem. Phys. **94**, 6644 (1991).
[67] U. Müller and G. Stock, J. Chem. Phys. **107**, 6230 (1997).
[68] M. D. Hack, A. W. Jasper, Y. L. Volobuev, D. W. Schwenke, and D. G. Truhlar, J. Phys. Chem. A **104**, 217 (2000).
[69] M. D. Hack and D. G. Truhlar, J. Phys. Chem. A **104**, 7917 (2000).
[70] P. L. Bartlett and A. T. Stelbovics, Phys. Rev. A **66**, 012707 (2002).
[71] M. Fárník, private communication.